

# Multitemporal characterisation of a proglacial system: a multidisciplinary approach.

Elisabetta Corte<sup>1</sup>, Andrea Ajmar<sup>2</sup>, Carlo Camporeale<sup>1</sup>, Alberto Cina<sup>1</sup>, Velio Coviello<sup>3,5</sup>, Fabio Giulio Tonolo<sup>4</sup>, Alberto Godio<sup>1</sup>, Myrta Maria Macelloni<sup>1</sup>, Stefania Tamea<sup>1</sup>, and Andrea Vergnano<sup>1</sup>

<sup>1</sup>Department of Environment, Land and Infrastructure Engineering, Politecnico di Torino, Turin, 10129, Italy

<sup>2</sup>Interuniversity Department of Regional and Urban Studies and Planning, Politecnico di Torino, Turin, 10125, Italy

<sup>3</sup>Research Institute for Geo-Hydrological Protection, CNR, Padova, Italy

<sup>4</sup>Department of Architecture and Design, Politecnico di Torino, Turin, 10125, Italy

<sup>5</sup>†deceased

**Correspondence:** Elisabetta Corte (elisabetta.corte@polito.it)

## Abstract.

The recession of Alpine glaciers causes an increase in the extent of proglacial areas ~~that and~~ leads to changes in the water discharge and sediment balance (morphodynamics and sediment transport). Although the processes occurring in proglacial areas are relevant not only from a scientific point of view but also for the purpose of climate change adaptation, there is a lack of studies on the continuous monitoring and multitemporal characterization of these areas. This work offers a multidisciplinary approach that merges the contributions of different scientific disciplines such as hydrology, geophysics, geomatics and water engineering to characterise the Rutor glacier and its proglacial area. We surveyed the glacier and its proglacial area since 2020 with ~~both uncrewed (drone)~~ uncrewed and crewed aerial ~~photogrammetric flights~~ surveys; we determined the bathymetry of the most downstream proglacial lake and the thickness of the sediments deposited on its bottom. Water depth at four different locations within the hydrographic network of the proglacial area and the bedload at the glacier snout were continuously monitored. The synergy of our approach enables the characterisation, monitoring and understanding of a set of complex and interconnected processes occurring in a proglacial area.

## 1 Introduction

Global warming is entailing a rapid decline of the cryosphere globally. ~~The mountain cryosphere, which consists of snow, ice, and permafrost, responds~~ Mountain snow cover and glaciers, respond directly and rapidly to climate change ~~and is a key indicator making them key indicators~~ of global warming. The ~~decline of the cryosphere exposes more land and water areas to solar energy, leading to decreasing albedo and to weathering, resulting in increased erosion. The~~ intensity and frequency of precipitation are ~~also changing due to climate change, whereas~~ changing and part of the precipitation has shifted from solid to liquid due to the increased temperatures (e.g. in the European ~~mountain~~ mountains). This shift and the increasing number of dry and warm winter days in European Alps reduce snow accumulation. In addition, rising air temperature in spring increases snow melt, modifying the local water balance (Carrer et al., 2023; Gizzi et al., 2022). Snowfall and ice/snow melt impact glacier

mass balance. As a consequence of global warming, the glaciers within the European Alps are subject to reduction in surface area and ice mass (Sommer et al., 2020).

25 Most glaciers reached their Holocene maximum extent at the end of the Little Ice Age (LIA) and have receded since then (Grove, 2004). With LIA being a cooler period in the Holocene, lasting from years 1300s to 1950s (Matthews and Briffa, 2005) ~~Glacier mass balance depends on several processes, including snowfall and ice/snow melt. At present, most Alpine glaciers are not in equilibrium with the current climate, so they are undergoing a dramatic mass loss. Glacier retreat is the most visible consequence of climate change. The impacts of global warming are severe for mountain areas because of their sensitive ecosystems, their topographic condition and the direct response of glaciers to climate change. Alpine glacier retreat is leading to~~  
30 increased exposure of formerly glaciated terrain, entailing the colonization of plants and animals, and changes in morphodynamics and sediment transfer. 1850s (Ivy-Ochs et al., 2009). The decline of snow cover and glaciers exposes more land and water surfaces to solar energy, leading to decreasing albedo and to weathering, resulting in increased erosion. Glaciers produce a considerable amount of sediments (Hallet et al., 1996), the size of which ranges in size from large boulders to fine sands, silt and clays (Hallet et al., 1996; Carrivick and Tweed, 2021). Depending on dynamic and thermodynamic conditions, glaciers  
35 have the ability to entrain sediment and erode bedrock. Even when the entrainment capacity is reduced, the glacier retains the ability to deform the sediment (Alley et al., 1997).

Using the terminology defined by Slaymaker (2011), the area encompassing the glacier outline at the end of the ~~Little Ice Age (LIA)~~ LIA and the present-day glacier terminus is the proglacial area. Proglacial areas are considered systems in transition from glacial to non-glacial conditions and are therefore natural laboratories that allow the investigation of the early  
40 stages of newly exposed soil development, vegetation succession, and associated soil stability and sediment fluxes (Matthews, 2019). Due to global warming and glacial retreat, disequilibrium occurs between sediment delivery from the glacier and fluvial reworking in proglacial areas (Slaymaker, 2011). Their evolution depends on the interaction between geomorphic processes and vegetation succession. On the one hand, plant colonization stabilizes glacial sediment and reduces sediment fluxes; on the other hand, geomorphic processes disturb and limit vegetation succession (Curry et al., 2006; Moreau et al., 2008; Eichel, 2019).

45 Studies investigating multiple processes within a proglacial area, on a larger scale than a single landform or a hillslope ~~for multiple times~~, at different time-frames are not frequent (Hilger and Beylich, 2019). The integration of all the processes involved in the sediment budget requires a catchment-wide identification, mapping, and quantification of all relevant sediment transport processes, a localization and monitoring of the storage elements in the sediment transport system, and a localization of their interaction areas (Hilger and Beylich, 2019). ~~Glaciers produce a considerable amount of sediment (Hallet et al., 1996), the size of which ranges in size from huge boulders to fine sands, silt and clays (Hallet et al., 1996; Carrivick and Tweed, 2021)~~  
50 ~~Carrivick and Tweed (2021) state that the remobilization of sediment within the proglacial area mainly determines sediment yield in a proglacial area. Guillon et al. (2018), in their study of the Bosson Glacier (FR), found that sediment sources vary according to season; sediment remobilisation within the sandur is the dominant source of sediment in autumn, while during the melt season the main export of sediment comes from the glacial source. Further efforts in integrating multiparametric~~  
55 observations and enhancing interdisciplinary scientific collaboration are needed to predict sediment dynamics in a warming world (Zhang et al., 2022)

Sediment availability is strongly governed by morphology (Cavalli et al., 2018). The land-system elements of a proglacial area have different geomorphic functions and are heterogeneously distributed. These elements can act like sediment sources, stores (short-term storage landforms) and sinks (long-term storage landforms) (Matthews, 2019). In Alpine catchments, runoff depends on rainfall events and snow and glacier melt (Camporese et al., 2014). Glacier ~~response to regional and retreat in~~ response to the local climate is heterogeneous in space and time (~~Carrivick and Tweed, 2021~~) and so is the water regime. Sediment yield depends on ~~water discharge runoff~~ and sediment availability which are both highly variable in space and time (~~Heckmann and Schwanghart, 2013; Hooke, 2000~~). ~~Moreover, the relationship between water discharge and both bedload~~ (Heckmann and Schwanghart, 2013; Hooke, 2000; Carrivick and Tweed, 2021). Furthermore, the connection among water discharge, bedload, and suspended sediment transport ~~can vary throughout exhibits variability over~~ the years and within ~~a season also due to climatic conditions~~ seasons, influenced by climatic conditions as highlighted in previous studies (Mao et al., 2018; Coviello et al., 2022).

In this work, to the best of our knowledge, we present the first public dataset of a proglacial area that is the result of hydrological, geophysical, geomatics and water engineering monitoring. This dataset is the result of a multidisciplinary approach and represents the input data to assess the water and sediment balance in the Rutor proglacial area and the morphodynamics occurring in recently exposed soils. The synergy among different disciplines has allowed for achieving a holistic viewpoint in the observation of the evolutive phenomena of the Rutor proglacial area.

## 2 Materials and methods

### 2.1 Site description

The Rutor glacier lies at the head of the Dora Baltea Valley in La Thuile, near the French-Italian border in northwestern Italy. It ~~has an area of 7,9 km<sup>2</sup> and is the third largest glacier in the Aosta Valley. The Rutor Glacier is considered one of the most representative glaciers due to its geographical position and its morphological and glaciological characteristics. It is~~ is mainly oriented to the northwest and ~~lies at an altitude ranging from 2540 m a.s.l. to 3486 m a.s.l.~~ Rocky ridges border the upper part of the glacier, and the "Vedettes du Rutor" divides the accumulation zone into two main cirques. Three ~~tongues form the glacier front, and the eastern one reaches the lowest altitude of the glacier,~~ with an average altitude close to the average value for Alpine glaciers, as retrieved from the Global Land Ice Measurements from Space (GLIMS) database (GLIMS Consortium, 2005; Raup et al., 2007). The Rutor glacier is among the glaciers with the largest surface area in the Alps, and it is the third largest glacier in the Aosta Valley (GLIMS Consortium, 2005; Raup et al., 2007). At present, it has a surface area of 7.5 km<sup>2</sup> and its front is formed by three tongues (Figure 1) :-

**a)** Digital Surface Model (DSM) as of 2008 of the Rutor glacier and the L4 lake catchment. The upslope area of L4 outflow (hatched area with continuous black lines) has been mapped using the 2008 model of Valle d'Aosta. The inset shows the location in Italy. **b)** DSM as of 2021 of the Rutor proglacial area and locations of L1, L2, L3 and L4 proglacial lakes.

~~Due to global warming, the Rutor Glacier has gone through a dramatic mass loss that were once united (Figure 2).~~ Villa et al. (2007) determined the Rutor glacier retreat and volume changes from the mid-19<sup>th</sup> century to 2004. Since 2005,

90 the regional environmental protection agency (ARPA) of Valle d'Aosta has been monitoring the mass balance of the Rutor glacier, which with the exception of the years 2013, 2014 and 2016 has always been negative, resulting in a cumulative mass balance from 2005 to 2017 of -12252 mm w.e. (ARPA Valle d'Aosta, 2014). Since its maximum Holocene extent in 1820 (Orombelli, 2005), when its surface area was about 12km<sup>2</sup> (Villa et al., 2007), it has lost extent in LIA (Orombelli, 2005; Villa et al., 2007), the glacier has lost approximately 34% of its surface area. Furthermore, a glacier retreat of about 1,5 km from 2005 to 2100,  
 95 has been evaluated by Strigaro et al. (2016) by considering RCP 8.5 climate scenario. Villa et al. (2007) also estimated the surface area and volume variations of the Rutor Glacier from its maximum expansion until 2004 (Figure 2), which offers an overview of the history of the glacier since the beginning of its recession. The retreat and lowering of the glacier surface are not uniform but more pronounced in the eastern tongue (Villa et al., 2007).

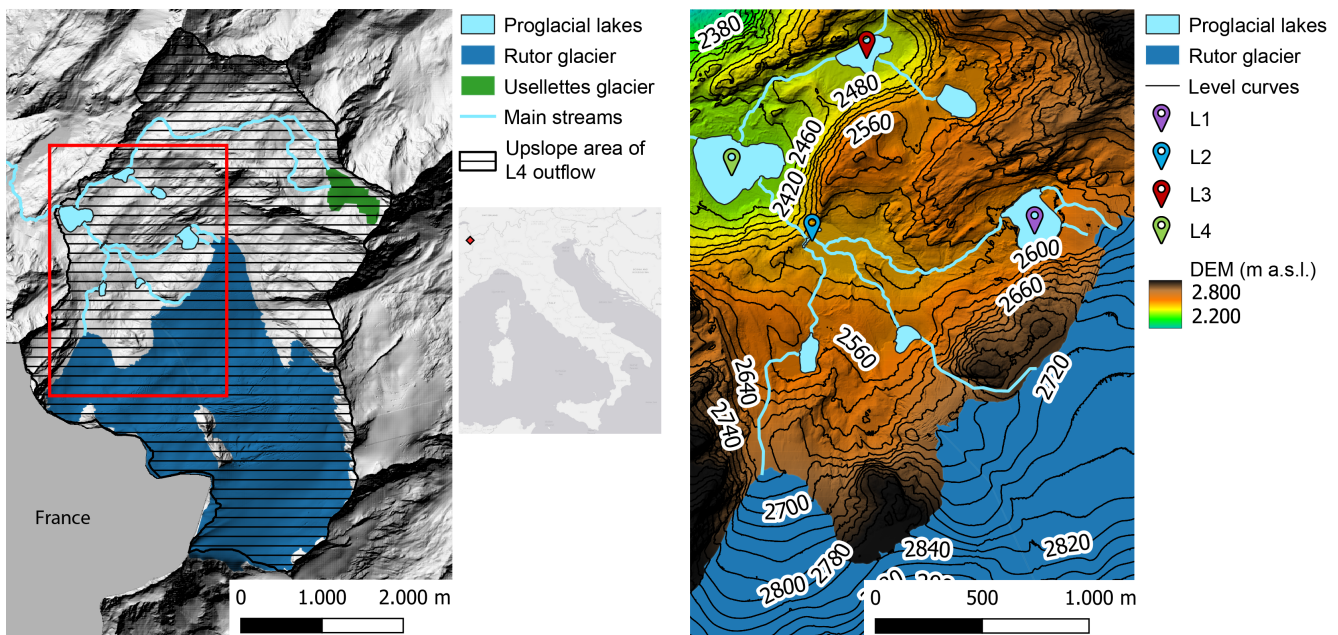


**Figure 1. a)** Hillshade based on the Digital Surface Model (DSM) as of 2008 of the Rutor glacier and the L4 lake catchment. The upslope area of L4 outflow (hatched area with continuous black lines) has been mapped using the 2008 model of Valle d'Aosta (SCT Geoportale, Regione autonoma Valle d'Aosta). The inset shows the location in Italy. **b)** DSM as of 2021 of the Rutor proglacial area and locations of L1, L2, L3 and L4 proglacial lakes.

The entire Rutor proglacial area ~~has an extension of about~~ spans approximately 4 km<sup>2</sup> (Villa et al., 2007) ~~and is of relevant~~  
 100 ~~interest for studying~~. This area holds significant importance for investigating sediment dynamics in proglacial systems ~~due~~,  
 owing to its geomorphological ~~heterogeneity, diversity and pristine condition resulting from minimal human impact. Notably,~~  
 the presence of L4, which acts as a basin closure within the proglacial area, collects all mobilized sediment within the region.  
 Since the end of LIA, the Rutor glacier has retreated, leading to a progressive ~~extension of its increase in the~~ proglacial area.  
 The glacier recession has exposed topographic depressions which determined changes in stream networks and the formation

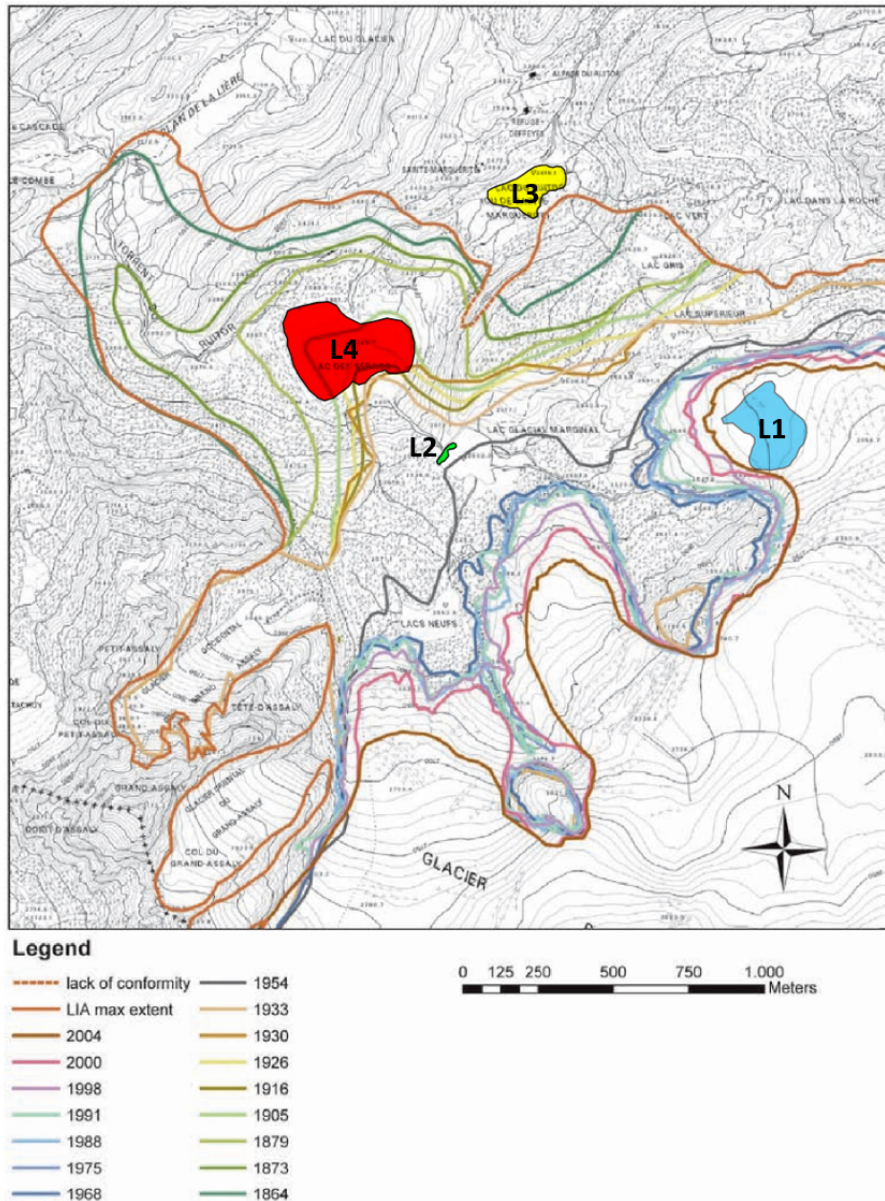


**Figure 2.** Reconstruction of the Rutor Glacier terminus from its maximum extent in LIA to 2004 (modified from Villa et al., 2007). The areas highlighted in blue, green, yellow and red indicate the current extent of lakes L1, L2, L3 and L4 respectively.

105 of several proglacial lakes. These lakes act as sediment sinks, interrupting sediment transfer from the glacier outlet to the lowlands. The altitude from the lowest proglacial lake to the glacier terminus (middle tongue snout) ranges from ~~2387~~ about 2390 m a.s.l. to ~~2661-2660~~ m a.s.l. The land-system elements within the Rutor proglacial area include steep slopes, outwash

plains (sandurs), and single and braided channels, while the alluvial channel beds and banks vary in size from fine sands, silt and clays to boulders.

110 ~~There are currently five proglacial lakes fed superficially by the eastern tongue of the glacier. Two of these have formed in the last five years and are attached to the glacier lobe. The third lake fed by the eastern tongue is L1 d (Figure 1), the second largest lake of the Rutor proglacial area. This lake has several inflows, but the main one comes directly from the eastern tongue of the glacier.~~ L1 has a single outflow which, after a distance of 830 meters, flows into a sandur. This sandur is fed by the meltwater of the entire glacier and has a surface area of about 0,1 km<sup>2</sup>. Due to a topographic barrier, the water is forced to  
115 flow downstream the outwash plain through a single channel. When the water level in the sandur rises, the above-mentioned topographic barrier determines the formation of the L2 lake (2504 m a.s.l.). The water flows from L2 to the L4 proglacial lake (Seracchi lake, 2387 m a.s.l.), through a steep creek with an elevation jump of about 100 m.

The outflows of L2 and L3 (Santa Margherita Lake) are the only two surface inflows of the L4 Lake, whose outflow feeds the majestic Rutor cascaades waterfalls. The L4 lake collects all meltwater from the Rutor glacier and is the major and the most  
120 downstream proglacial lake of the analyzed area. Its outflow cross-section is quite stable and allows to easily measure the lake outflow. Since the main processes involving the water and sediment budget of the Rutor proglacial area occur upstream and within L4, the study focuses on the basin area upstream of the outflow control section of L4, with an overall catchment area of 18,12 km<sup>2</sup>, whose 4443% is glacierized (Figure 1).

The characteristics of the study area described above can be easily observed through a WebGIS available at <https://arcg.is/Tyeju0> (last access: ~~17 January~~ 10 November 2023).  
125

Among all the lakes of the area, the Santa Margherita Lake ~~;~~ here named L3 ~~;~~ (2422 m a.s.l.) ~~;~~ was the most monitored in the past, because of catastrophic outburst floods (Baretti, 1880; Sacco, 1917), which began in the first half of the XV century, showing that the glacier at the time had already retreated (Sacco, 1917).

The past evolution of L3 lake testifies the changes that the whole area had gone through due to the glacier retreat since the  
130 end of the LIA. These changes have been reported in several documents (e.g., Sacco, 1917; Baretti, 1880; Valbusa and Peretti, 1937), that allow reconstructing the changes of the glacier and its proglacial area.

## 2.2 Multidisciplinary framework

The assessment of the water balance and sediment budget implies the identification of the different physical processes involved, their geomorphic function ~~and their proportional,~~ their contribution to the overall sediment production and their effectiveness  
135 in supplying sediment to the mainstream (Hilger and Beylich, 2019). ~~The number of~~ Quantifying the sediment budget of proglacial areas is a challenging task due to the multitude of processes involved and their spatial and temporal variability ~~makes quantifying the sediment budget of proglacial areas challenging.~~ Most studies either focus on a single landform or hillslope at different times (e.g., Laute and Beylich, 2014; Curry et al., 2006), or they measure river-basin scale production rates at the outlet of the basin (e.g., Hicks et al., 1990; Müller, 1999; Bogen et al., 2015). The following paragraph provides a concise  
140 overview of the monitoring methods used in three distinct studies concerning different proglacial areas.

Guillon et al. (2018) combined sedimentary measurements with precipitation data to understand present-day suspended sediment storage and erosion processes during ~~one melt season in the Bosson glacier proglacial area~~ melt season. They measured water depth and turbidity, deriving water discharge and suspended sediment concentration respectively, in three different stations ~~within the proglacial area~~. Orwin and Smart (2004) characterized a proglacial channel over a 9-week ablation period by continuously measuring the water depth and turbidity in ~~nine~~ different gauging stations distributed within the proglacial area. ~~Their study confirmed~~ Confirming that sediment yield varies spatially and temporally within a proglacial area. Delaney et al. (2018) assessed erosion rates and processes in ~~Griesgletscher's proglacial area~~. ~~That glacier is located near a hydropower infrastructure so the catchment has been monitored annually since 1986. To determine volume changes and assess sediment processes in Griesgletscher's proglacial area they used~~ an alpine proglacial area through digital surface models (DSMs), reservoir bathymetry and a glacial-hydrological model (GERM). Water discharge measurements were determined by the ~~reservoir's water level~~. ~~Guillon et al. (2018) and Orwin and Smart (2004) measured both discharge and turbidity at different locations in the proglacial area, providing~~ water level at the reservoir located at the basin outlet. The first two reported studies (Guillon et al., 2018; Orwin and Smart, 2004) provided an explanation for the variation in space and time of proglacial suspended sediment flux but they did not assess the landscape evolution of the geomorphological features in ~~proglacial areas. However, although Delaney et al. (2018) identified the~~ the whole proglacial area, whereas in the latter reported study (Delaney et al., 2018) the sediment processes in the ~~proglacial area using DSMs, they measured water discharge whole~~ proglacial area was identified but the water discharge was directly measured only at the basin outlet. The studies presented are of important value for the understanding of the dynamics in proglacial areas, but there is a lack of studies in the literature involving repeated surveys (e.g. photogrammetric flights) and continuous monitoring (e.g. flow measurements) at several points in the proglacial and glacial area.

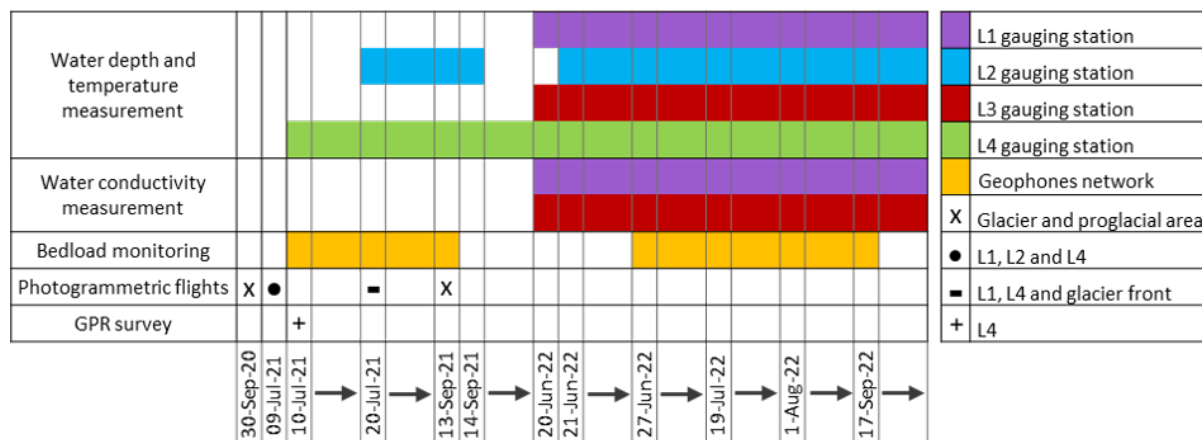
Since ~~2004, the environmental agency ARPA~~ 2005, the local environmental agency (ARPA) of Aosta Valley has been monitoring the mass balance of the Rutor glacier through direct in situ measurements. Starting from 2020, the Glacier Lab of the Turin Polytechnic integrated ARPA surveys with geophysical and geomatics measurements. Since the summer of 2021, the area monitored by the Glacier Lab has increased from 25.2 to 34.5 km<sup>2</sup> to include the proglacial area.

~~The~~ Our monitoring activities at the Rutor glacier can be categorized into multitemporal and continuous surveys. An overview of these monitoring activities is provided in ~~table~~ Table 1.

### **2.2.1 Geomatic survey: aerial acquisitions and GNSS positioning**

The Rutor glacier was monitored with different geomatics techniques supported by different surveying campaigns, with two aims: i) to provide a common 3D reference system to properly manage all the spatial and temporal datasets of the different research groups involved in the glacier monitoring, and ii) to enable the 4D (3D over the time) monitoring of the extent and morphology of the glacier surface. The geomatics surveys started in 2020 and include both uncrewed (~~drone~~) and crewed aerial photogrammetric flights as well as topographic measurements in the field. ~~As far as the~~ The geomatics surveys were carried out in parallel with the activities of the other Glacier Lab teams, to acquire in-situ data and enable the implementation of integrated multidisciplinary monitoring activities.

**Table 1.** Timetable of continuous measurements and field surveys, in the first column the measured quantities/surveys and at the bottom the timeline. Each colour and symbol are characteristic of the measuring station and surveyed area respectively. The arrows between the dates indicate that the measurements are continuous between the dates.



175 In the 2020-2021 period is concerned, the following surveys, the surveys described in Table 2 have been carried out: Aerial flights: 30<sup>th</sup> September 2020 and 13<sup>rd</sup> September 2021, over the whole area Drone flights: . Among those, during the summer campaigns in 2021, three photogrammetric flights (one in 9<sup>th</sup> July 2021 and two in 20<sup>th</sup> July 2021, over the proglacial area A summary of the flight coverage and technical features is included in Table ??) were carried out with the DJI Phantom 4 RTK UAV multirotor platform (using the UAV's built-in camera equipped with a 1" RGB sensor) to survey the proglacial lakes.

**Table 2.** Photogrammetric flights carried out on the study area between 2020 and 2021.

Photogrammetric flight	Date of acquisition	Covered area	Extent (km <sup>2</sup> )	Average flight height (m)	GSD (m)	Number of Images	Number of GCPs	Number of CPs
Aerial	30/09/2020	Glacier and a portion of the proglacial area	25.2	818	0.07	867	18	7
~	~	~	~	~	~	~	~	~
Drone-UAV	9/07/2021	L1, L2 and L4	2.6	126	0.03	1480	6	6
Drone-UAV	20/07/2021	L1 and L4	0.4	89.2	0.02	369	6	2
Drone-UAV	20/07/2021	Glacier front and lower part	1.1	159	0.04	623	Direct georeferencing	Direct georeferencing
~	~	~	~	~	~	~	~	~
Aerial	13/09/2021	Glacier and proglacial area	34.5	877	0.06	1100	9	4
~	~	~	~	~	~	~	~	~



180 ~~The geomatics surveys were carried out in parallel with the activities of the other Glacier Lab teams, to acquire in-situ data and enable the implementation of integrated multidisciplinary monitoring of the Rutor Glacier.~~

~~More specifically, during the summer campaigns in 2021, three photogrammetric flights (one in 9<sup>th</sup> July 2021 and two in 20<sup>th</sup>) were carried out with the DJI Phantom 4 UAV multirotor platform (using the drone's built-in camera equipped with a 1" RGB sensor) to survey the proglacial lakes (see Table ??).~~

185 After the summer of 2021, at the end of the hydrological year 2020/21, ~~manned-crewed~~ photogrammetric flights were carried out by the Digisky company over the glacier and proglacial area, using a medium-format PhaseOne camera iXM-RS150F installed onboard an ultralight aircraft. The crewed aerial flight was carried out with a P90e light aircraft. Its handling allows easy flight altitude changes to maintain a constant GSD. The camera has a focal length of 50 mm, a sensor size of 40 x 53.5 mm and a resolution of 151.3 MP. ~~More flights were needed to ensure cloud-free coverage of the glacier area.~~ The 2021  
190 photogrammetric survey was the repetition of a previous flight, carried out at the end of September 2020 with the same aerial platform and sensors but with a smaller coverage (without a complete coverage of L2, L3 and L4 lakes).

During the ~~activities in the field~~, a set of 2021 field activities, a total of 32 artificial photogrammetric markers, either squared (0.5 m x 0.5 m) plastered markers or crosses painted on stable rocks, were positioned (or painted) and measured with a Real-Time Kinematic (RTK) and static Global Navigation Satellite System (GNSS) positioning approach, using 3 Spectra  
195 Precision SP80 GNSS receivers (static data have been processed with RTKLIB software). The markers were distributed on the periglacial-proglacial area (to ensure stability over time), around L4 and along the L1 until the glacier front on the eastern tongue. ~~Moreover, around the top part of the glacier area, a set of~~ Among the 32 markers, 12 larger markers (1 m x 1 m markers  
) were positioned during the September 2021 campaign around the top part of the glacier area, to enable a straightforward identification on aerial images.

200 ~~Unlike drone flights which were oriented exploiting~~ The markers placed in 2021 have been used as both GCPs and independent CPs (details in Table 2) for the 2021 crewed aerial survey. Considering that the focus is on relative displacements rather than on absolute values, 25 natural GCPs and CPs have been then identified on the 2021 orthomosaic and DSM to orient the 2020 crewed aerial imagery and assess its 3D positional accuracy (considering that the artificial markers were not yet available in 2020). A GPC/CP based approach has been used also for UAV surveys, except for one UAV survey where, exploiting the  
205 RTK capabilities of the UAV GNSS receiver, a direct georeferencing approach ~~,the~~ has been adopted (considering it was not possible to place markers in the glacier front for safety reasons). Direct Georeferencing refers to the orientation of remotely sensed imagery without using GCP, exploiting Real Time Kinematic (RTK) or Post Processing Kinematic (PPK) approaches. The RTK- or PPK-based approach enables the generation of metric products with 3D positional precision and accuracy in the range of few centimeters (Chiabrando et al., 2019; Teppati Losè et al., 2020a, b).

210 Since the camera positions of aerial flights were not geo-tagged with proper accuracy. ~~It was, therefore,~~ it was necessary to exploit the artificial markers to georeference the 3D model accurately over the entire glacier area. The cartographic reference system adopted for all the 3D models is ETRF2000/UTM32N; the ellipsoidal height was reduced to orthometric height by applying the Italian geoid model ITALGEO05. Due to ~~a large~~ the availability of a suitable number of well-distributed ground control points, the 2021 aerial survey was considered the reference model (referred to as 'Model Zero') to be used for multi-

215 temporal analyses. The 2020 survey was, therefore, co-registered (i.e., georeferenced in the same reference system, enabling the overlap of all the derivative products) with the 2021 survey.

~~To assess the advantages and disadvantages of a multiplatform, multiscale and multitemporal analysis, a Pleiades very-high-resolution satellite stereo-pair acquired in 2017 was also used. The satellite multispectral imagery (including visible and near-infrared data with a nominal GSD of 0.71 m resampled to 0.50 m) was processed to extract two orthoimages and one DSM. Since the main~~  
220 objective is the evaluation of relative displacements, the DSMs were compared using a pixel-by-pixel approach. In particular, the height of DSM 2021 (i.e. the pixel value) was subtracted from that of DSM 2020. The overall comparison allows the evaluation of changes in the glacier surface, while the comparison limited to stable areas allows further validation of the elevation products. Stable areas were defined as those not covered by ice, snow or water. Outwash plains, which may have been affected by geomorphological changes (e.g. due to erosion and water deposits) between the time of the surveys, were also  
225 considered stable areas. These areas were included to obtain a statistically relevant comparison dataset. The stable areas were used for relative validation, therefore considering areas that may have changed between the time of the surveys is conservative, as it could worsen the statistics.

### 2.2.2 Geophysical survey

The bathymetry of Seracchi Lake and the thickness of the sediments deposited on its bottom were determined by using a  
230 Ground Penetrating Radar (GPR) (Sambuelli et al., 2015) supported by Time Domain Reflectometry (TDR) measurements (He et al., 2021), as reported in more detail in Vergnano et al. (2023).

Both systems are based on the principle of the propagation of high-frequency electromagnetic signals, in the bandwidth between 30 MHz and 1 GHz. The signal propagation in natural media depends on the electromagnetic properties of the media (dielectric permittivity and electrical conductivity). In a low-conductivity material, the signal propagates with a velocity related  
235 to the dielectric permittivity, according to  $v = c/\sqrt{\epsilon}$ , where  $c$  is the electromagnetic wave velocity in vacuum and  $\epsilon$  is the relative dielectric permittivity of the material (Psarras, 2018). The velocity is usually estimated in the time domain: a signal pulse is excited by an antenna (in GPR) or TDR device, and it propagates into the medium; part of the energy carried out by the signal is scattered back (or reflected) when a contrast of electromagnetic impedance is encountered. The amount of energy that is reflected depends on the contrast of electrical conductivity or dielectric permittivity between two different media. The  
240 backscattered signal is then collected by an antenna (receiving antenna in GPR) or by an oscilloscope in the case of TDR devices. In the GPR, the amplitude of the signal that is backscattered at the interface between two different media defines the reflectivity of the target. The GPR approach for detecting the bathymetry of a lake is based on the reflectivity of the lake bottom, based on the contrast of dielectric permittivity between water and sediments of the lake bottom.

The dielectric permittivity of water depends on the temperature, and it is slightly affected by salinity; typical values at low  
245 temperatures are around 80 (relative values, referring to the dielectric permittivity of vacuum), corresponding to an e.m. waves velocity in water of around 0.033 m/ns. In our case, with a 6-degree temperature and a relative permittivity of 83.3, the wave velocity was estimated to be 0.0327 m/ns. High porosity sediments could exhibit dielectric permittivity in the range between

35 and 40. This means that the water-sediments interface should exhibit good reflectivity, given the contrast of dielectric permittivity values.

250 The GPR antenna, [manufactured by IDS GeoRadar s.r.l.](#), had a central frequency of 200 MHz, which provides the best possible resolution while avoiding the energy dispersion that occurs in water at frequencies higher than 200 MHz (Bradford et al., 2007). The GPR system was installed on an inflatable rowing boat and the boat was moved to cover the whole area of the lake. The ~~analysis of the GPR travel times provided the sections of the water depth and sediment thickness, which were interpolated into a bathymetric model~~[GPR sections acquired were processed according to a set of standard processing steps, performed in Reflexw software \(Sandmeier, 2021; Vergnano et al., 2023\), and reported in Appendix B.](#)

255 [The x-y-z locations of the first interface, representing the lake bottom, detected in all the GPR sections, were interpolated with a linear triangulation-based method \(griddata function of MATLAB\) to produce a bathymetry map \(Figure 11, which also displays the sediment thickness distribution and the electrical conductivity measurements\). The perimeter of the lake, retrieved from the 6-cm-resolution orthophoto acquired on the day of the geophysical survey, was useful to fix the 0-depth in the interpolation process.](#)

260 The TDR probe, installed on a rod, was inserted in the lake bottom sediments at several locations and measured their electrical conductivity and dielectric permittivity. The valence of the TDR survey is double:

- to corroborate the interpretation of the GPR sections, because the punctual values of dielectric permittivity give an estimation of the electromagnetic wave velocity in the sediment ( $v$ ), necessary to convert the GPR travel times into thickness of the sediments itself. Also, the dielectric permittivity can be used to define the expected reflectivity of the water-sediments interface and to estimate the sediment porosity, since they are considered fully saturated.
- to assess the spatial variability of the type of sediments by measuring their electrical conductivity. In fact, the electrical conductivity of the lake sediments depends on the porosity, water salinity and temperature, and texture of the sediments; the electrical conductivity is a good indicator of the presence of finer material, as the bulk electrical conductivity usually increases due to the contribution of the surface electrical conduction of the finer particles.

270 To validate the GPR and TDR measurements, geotechnical analyses (grain size distribution and Atterberg's limits) were performed on a few sediment samples collected at the locations shown in Figure 11 ([see Vergnano et al. \(2023\) for more details](#)).

### 2.2.3 Hydraulic monitoring

275 The hydrography of the Rutor proglacial area is made complex by a sequence of flat and steep areas, by the presence of several proglacial lakes differently connected and by the contribution from three tongues of the glacier. In order to assess the partial and total [surface](#) runoff, four instruments were installed to measure the water depth at different locations in the study area. The location of these water pressure gauges was determined by the accessibility and the geometry of the channel or lake and the presence of stable rocks or banks on which to install the instruments.

280 Two types of instruments were installed: i) a self-contained, water logger and transmitter measuring water level and temperature (OTT ecoLog 1000); ii) a combined measurement of water level, temperature, and conductivity (OTT CTD). The four locations of the gauging stations, from upstream to downstream, are L1 emissary, L2, L3 emissary, and the outflow of L4 (Figure 3). Water depth allows one to retrieve from direct velocity measurements the water discharge, and conductivity measurements allow water characterization for surface or groundwater flow, which is a matter of interest for L3 and L4. Therefore, 285 the two OTT CTDs were installed in L1 and L3 emissaries. [The ecoLog1000 and CTDs instruments were first installed in July 2021 and June 2022, respectively; the measuring periods of each sensor are shown in Table 1.](#)

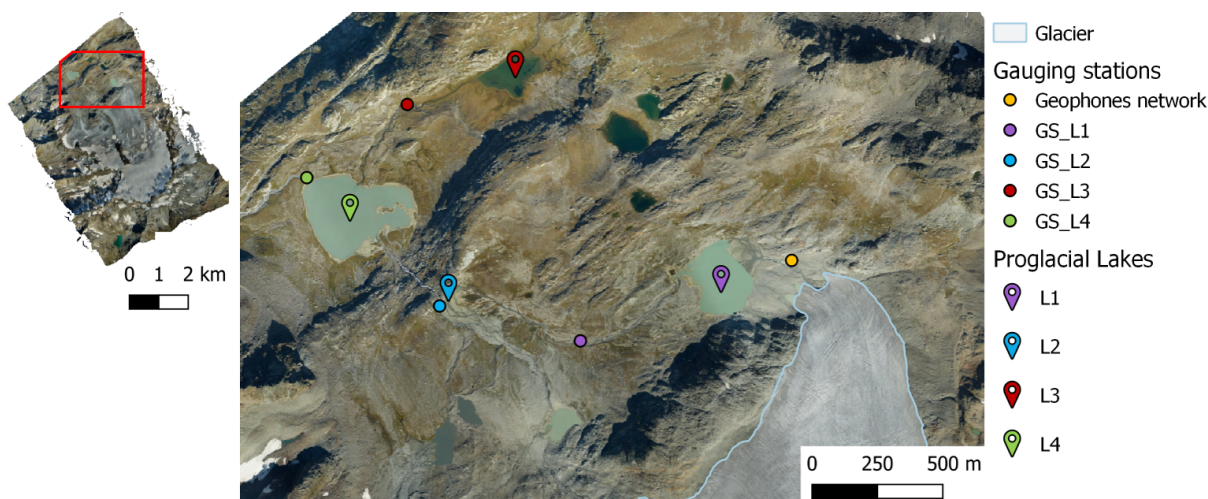


**Figure 3.** [Orthophoto-Aerial orthophoto](#) of the Rutor proglacial area [acquired on 13/09/2021](#) and the snout of the Rutor eastern tongue. The red polygon in the upper left orthophoto shows the position of the area enlarged in the right figure. The lakes (L1,L2,L3 and L4), the gauging stations and the geophones network are indicated.

The upslope areas of the 4 sensors installed are: [-3-5.3 km<sup>2</sup>](#) for L1 gauging station, [-6-12.6 km<sup>2</sup>](#) for L2 gauging station, [-9-4.9 km<sup>2</sup>](#) for L3 gauging station, [and 18 km<sup>2</sup>](#) for L4 gauging station.

290 Since the area covered by the photogrammetric [flight-flights \(2020 and 2021\)](#) excluded a portion of the upstream area of L1 and L3 gauging stations, these areas were determined using the 2008 DSM of Aosta Valley [-available-at-\(last-access:-17-January-2023\)](#) [\(SCT Geoportale, Regione autonoma Valle d' Aosta\).](#)

295 At all the cross sections of the gauging stations, with the exception of L2, the flow velocity was measured with a current meter. At L2, due to the high flow velocity during the summer season, direct measurements are not safe for the operator. To derive the discharge from the water level measurements, a stage-discharge (or rating) curve has to be developed. [Flow-In the summer of 2021 and 2022, a set of nine flow](#) velocity measurements were taken with an Acoustic Doppler Velocimeter (ADV) current meter in the cross-section of gauging station L4 [for a total of 9 surveys.](#) [The velocity-based discharge measurements  \$Q\$  were related to the corresponding water depth  \$h\$  measured at the gauge \(Figure 4\), to plot the stage-discharge diagram \(Figure 5\(a\), further details on the procedure are given in Appendix A\).](#)

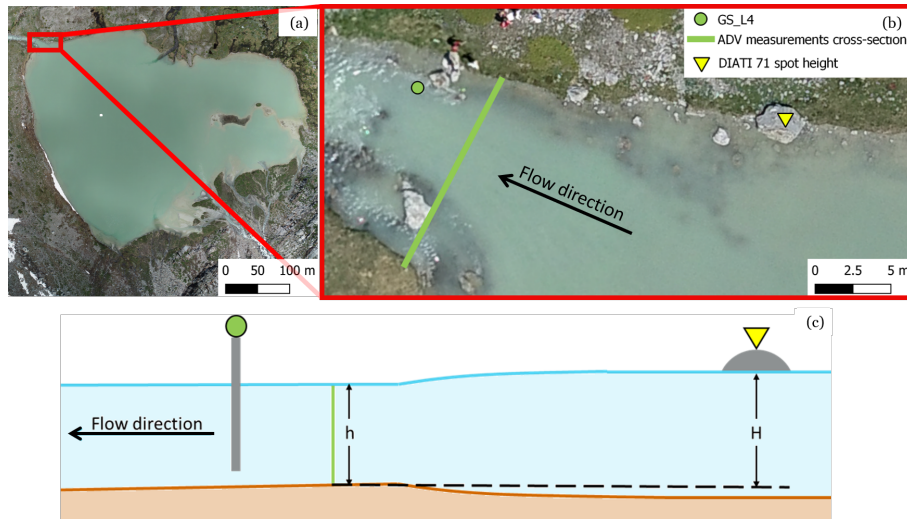


**Figure 4.** (a) Orthophoto of L4 (July 2021); (b) zoom in of the L4 outflow where the ADV measurements were taken and the DIATI 71 spot height is shown; (c) the longitudinal cross-section of the L4 outfall shows the reference water depth of the emissary ( $h$ ) and the reference total head measured in the lake ( $H$ ).

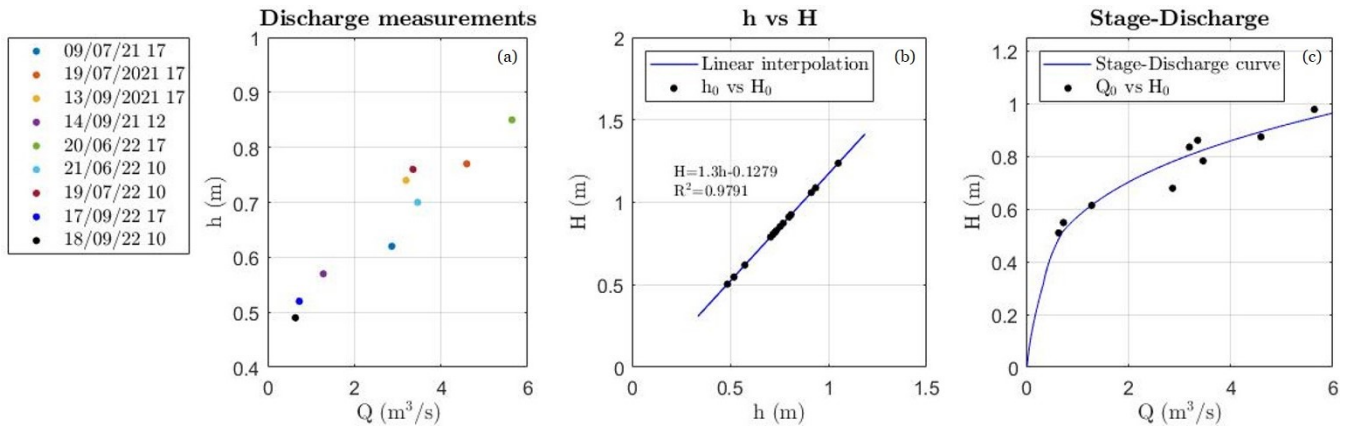


**Figure 5.** In the left-hand figure an Orthophoto of L4 with a red rectangle indicating the location of the enlarged area (a) Discharge measurements in the right-hand figure. In the latter, the L4 measuring station, the cross-section where the ADV measurements were taken emissary and the DIATI 71 spot height are shown corresponding water depth ( $h$ ). In the bottom figure, the longitudinal cross-section (b) Measurements of total head  $H$  and the L4 outfall shows the reference corresponding water depth of  $h$ . The linear interpolation equation and the emissary coefficient of determination ( $hR^2$ ) are reported. (c) Discharge measurements and the reference corresponding total head measured in the lake ( $H$ ) and the stage-discharge curve for L4 emissary.

L4 is the largest and the most downstream lake of the area collecting the whole meltwater of the Rutor ~~Glacier~~ glacier and the suspended sediment of the upstream area. Monitoring the water level and the outflow of L4 is crucial to assess the water and sediment budget of the Rutor proglacial area. ~~To monitor the water level~~ Due to backwater effects at the outflow, the water levels in the lake ~~;~~ the and the control cross-section are not identical, but strictly related. Therefore, to monitor the lake's stage, a relationship between the ~~water level recorded continuously in the L4~~ continuously recorded water level at the gauging station and the water level in ~~L4~~ the lake far from the gauging station was determined. A spot height was placed on a rock near the shore of the lake (Figure 4); the water level of the lake was assessed by measuring the altitude difference with the spot height (DIATI 71) using a laser level and a levelling staff. A total of 15 altitude difference measurements were taken during the 2022 summer campaigns. The ~~position of the instrument~~ instrument's position at L4 gauging station and the geometry of the L4 outfall cross-section were measured with ~~a~~ an RTK positioning approach (Table 3). This made it possible to determine the position of the measuring point of the instrument and to establish a reference elevation against which to assign the water depth in the outfall cross-section ( $h$ ) and the water depth in the lake ( $H$ ). The elevation of the bed of the L4 emissary, where the ADV measurements were taken, is considered the reference elevation; the water depth in the outfall ( $h$ ) and ~~in~~ L4 ( $H$ ) was assessed by subtracting the orthometric elevation of the bed of the L4 emissary from their geodetic elevation.

**Table 3.** Orthometric height of spot height DIATI 71, L4 gauging station measuring point and reference elevation.

	Orthometric height (m a.s.l.)
DIATI 71	2388.14
Measuring point at L4 gauging station	2386.50
Reference elevation	2386.12

The best fitting of the relation between the water depth measurements at the gauge  $h$  and the Hydraulic head in the lake  $H$  was found to be linear ( $H=1.3h-0.1279$ ,  $R^2 \sim 0.98$ ; see Figure 5(b)). The stage-discharge diagram ( $h$ - $Q$ ) and the linear fitting ( $h$ - $H$ ) were used to calibrate the lake outflow curve, i.e., the relationship between the hydraulic head ( $H$ ) in the lake and the flowing discharge ( $Q$ ) (Figure 5(c)).

#### 2.2.4 Bedload monitoring

Quantitative sediment transport estimation in proglacial streams is challenging due to frequent geomorphic changes associated with snow cover/melt and glacier dynamics. A growing number of studies investigate the use of seismic techniques to obtain continuous, indirect measurements of bedload transport (e.g., Bakker et al., 2020; Coviello et al., 2018; Schmandt et al., 2013). Geophones installed near a stream channel detect seismic waves produced by two different seismic sources: coarse particles impacting on the channel bed and flow turbulence. We use a low-cost and easy-to-install geophone network to investigate the temporal variability of the hydro-sedimentary export from the snout of the Rutor glacier. Data are recorded with a DATA-CUBE3 (solar power supply, 24-bit converter, GPS-based time synchronization) ~~with~~ configured with an amplifier gain of

325 [16, with](#) a sampling frequency of 200 Hz and stored on site. On 10 July 2021, we deployed a temporary monitoring network composed of three single-component geophones (4.5 Hz) installed along the proglacial stream draining the eastern tongue of the Rutor glacier. The geophones were installed a few meters from the right bank of the channel, about 200 m downstream of the glacier snout (Figure 6). The monitored channel reach (main channel in Figure 6) features a wetted perimeter of about 10 m and a slope of 2°. An ephemeral stream channel crosses the area monitored by Geo 1, which is the sensor located at  
330 the smallest distance from the main channel, (about 3 m). This ephemeral stream is a tributary of the main channel and likely activates during intense rainstorm events. On the other side of the ephemeral stream are installed Geo 2 and Geo 3, at a distance of 6 m and 8 m from the main channel, respectively.

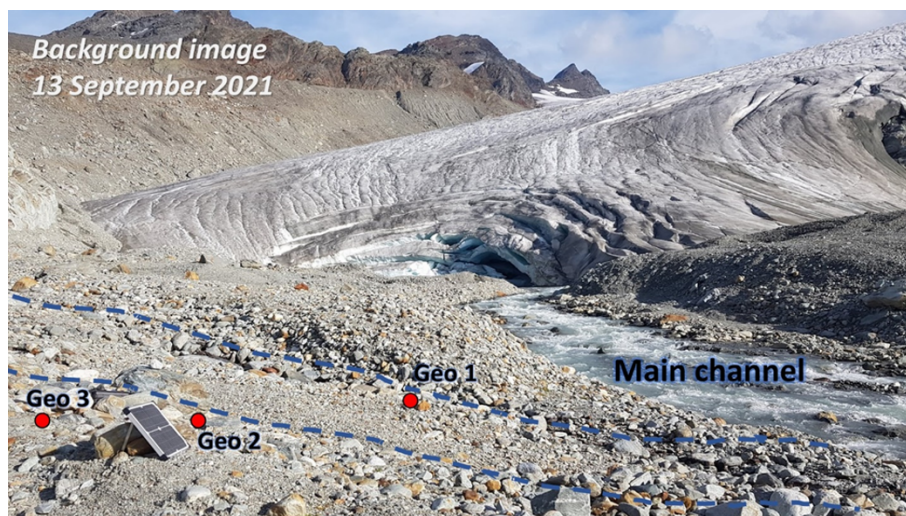


**Figure 6.** View on the monitored reach of the proglacial stream draining the eastern tongue of the Rutor glacier. Red dots indicate the location of the geophones, and the dashed blue line is the limits of the ephemeral stream flowing into the main channel.

[The counts exported by the DATA-CUBE3 are converted to vertical ground velocity considering logger and geophone sensitivities according to the manufacturer's specifications. The power spectral density is determined as the ratio of the square of the absolute value of the Fourier transform to the time window \(Bakker et al., 2020\). Raw seismic signals were filtered in the band 5-95 Hz and then the envelope was calculated as the average of the absolute value of the filtered signal over a time window of 1-min.](#)  
335

[During the 2022 season, we performed direct measurements of bedload transport at the glacier mouth by means of portable samplers during a day of intense glacier melt \(14 July\) and at the end of the monitoring season \(16 September\). Bedload traps \(4 mm mesh size, 20 × 30 cm opening, \(Bunte et al., 2004\)\) were deployed simultaneously at 2 positions. Measured unit bedload rates feature a large variability ranging from 0.02 to 16.2 kg/m/min in a few hours, as already observed in glacierized basins \(Coviello et al., 2022\). Bedload samples were sieved and weighed to obtain the grain size distribution. The total bedload transport rate  \$Q\_s\$  \(kg/min above 4 mm\) for each sampling period \(ranging from 2 to 30 min\) was estimated as width-weighted averages based on the available positions sampled.](#)  
340

### 345 3 Results

The dataset derived from the results presented in the following sections is also accessible in a WebGIS (available at <https://arcg.is/Tyeju0>, last access: ~~17 January~~ 10 November 2023) through which it is possible to find the link to the open repository according to the location of the monitored/surveyed point.

#### 3.1 Orthophotos and DSMs products

350 The images acquired with the photogrammetric ~~drone-UAV~~ and aerial flights were processed to obtain a 3D model of the terrain and additional cartographic products, i.e. orthophotos and DSMs. ~~The use of a Rover Base System and the presence of measured markers enabled the extraction of~~ A standard Structure-from-Motion (SfM) photogrammetric approach was adopted, following a consolidated workflow (i.e. interior and exterior orientation, camera calibration, dense point cloud generation, DSM and orthomosaic generation) using the software Agisoft Metashape. Table 4 shows the planimetric and altimetric errors  
355 calculated on both GCPs and CPs. The “reference” dataset is characterised by a planimetric accuracy (CPs) of 7.7 cm and a vertical accuracy of 11.1 cm. The 3D data with centimetric accuracy (including the vertical component) . accuracies of the other datasets are calculated considering the 2021 drone dataset as ground truth.

**Table 4.** Planimetric and altimetric errors calculated on both GCPs and CPs.

<u>Flight</u>	<u>Number of GCPs</u>	<u>Number of CPs</u>	<u>Residuals GCP</u>		<u>Residuals CPs</u>	
			<u>[cm]</u>	<u>[cm]</u>	<u>[cm]</u>	<u>[cm]</u>
			<u>RMS hor</u>	<u>RMS ver</u>	<u>RMS hor</u>	<u>RMS ver</u>
<u>Aerial 2021</u>	<u>9</u>	<u>4</u>	<u>4.7</u>	<u>6.1</u>	<u>7.7</u>	<u>11.1</u>
<u>Aerial 2020</u>	<u>18</u>	<u>7</u>	<u>24.3</u>	<u>10.6</u>	<u>9.5</u>	<u>16.7</u>
<u>UAV 9th July 2021</u>	<u>6</u>	<u>6</u>	<u>2.6</u>	<u>1.9</u>	<u>5.4</u>	<u>7.8</u>
<u>UAV 20th July 2021</u>	<u>6</u>	<u>2</u>	<u>22.7</u>	<u>8.8</u>	<u>1.8</u>	<u>1.5</u>

2021 UAV orthoimages and DSMs have a ~~2D~~ spatial resolution lower than 0.04 m 4 cm; the mosaic of such metric products provides a very detailed model of the area covering the path of the water melted from the eastern glacier tongue towards the  
360 periglacial-proglacial lakes (Figure 7, right).

~~Aerial orthophoto as of September 2021 (left) and Drone high-resolution mosaic of orthophotos of 9<sup>th</sup> and 21<sup>th</sup> July 2021 (right)~~

The spatial resolution of 2020 and 2021 aerial orthoimages have a slightly lower spatial resolution (about 0.07 m) with respect to drone is slightly lower (around 7 cm) compared to UAV ones, while the aerial DSMs have a spatial-resolution of  
365 about 0.2 m. Figure 7 clearly shows the larger coverage of the aerial orthoimage (left) with respect to the ~~drone-UAV~~ one (right).



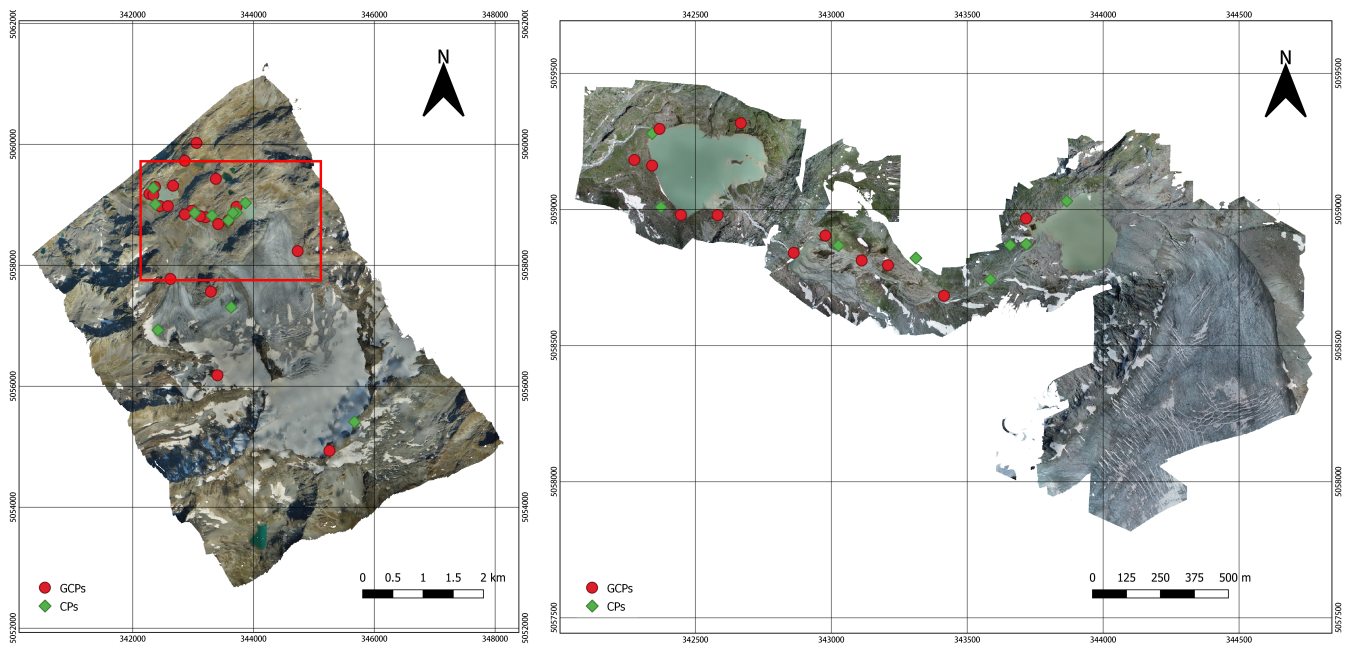


**Figure 7.** Aerial orthophoto as of September 2021 (left) and UAV high-resolution mosaic of orthophotos of 9<sup>th</sup> and 21<sup>th</sup> July 2021 (right)

A multi-temporal analysis was carried out by means of i) a comparison of ~~drone~~ UAV and aerial orthoimages to highlight the eastern glacial front retreat and ii) a difference of the aerial DSMs to estimate glacier surface elevation differences. Both analyses confirmed that the eastern tongue is the one undergoing the most significant mass loss and an apparent front retreat.

370 The multitemporal orthoimage comparison (of the Eastern glacial front was performed considering additional datasets to the ones previously described, namely a) the 2012 color orthomosaic available as WMS through the Italian national geoportal (<http://www.pcn.minambiente.it/mattm/>, last access: 09 November 2023) and b) a Pléiades orthophoto acquired in August 2017. Figure 8 ~~, including additional data sources in different years~~) shows that the front is receding annually. ~~The~~ the glacier tongue front has receded by more than 200 m in 9 years ~~(archive dataset acquired in 2012 available at , last access: 17 January 2023)~~ and about 100 m from 2017 to 2021.

380 ~~The aerial DSMs were preliminary compared to the LiDAR DSM as of 2008 available on Valle d'Aosta Geoportal to verify the consistency of the produced model, checking the stability of the periglacial rocky areas. Subsequently, 2021 and Glacier surface elevation differences were estimated by subtracting 2021 DSM to 2020 DSMs were subtracted one,~~ to quantify glacier ablation and displacement (~~Figure 9~~ Table 5). The comparison of 2020 and 2021 aerial DSM showed considerable subsidence in the lower part of the glacier, with a marked decrease in glacial volume. ~~The~~ When comparing two DSMs (i.e. Difference of DSMs, DoD) it's crucial to distinguish the information (actual vertical displacement) from the noise. To this purpose, the Limit of Detection approach has been adopted. The vertical error of the two DSMs propagates when calculating their difference. From the RMS of the DSM, it is possible to calculate the RMS of the difference exploiting the error propagation theory. The

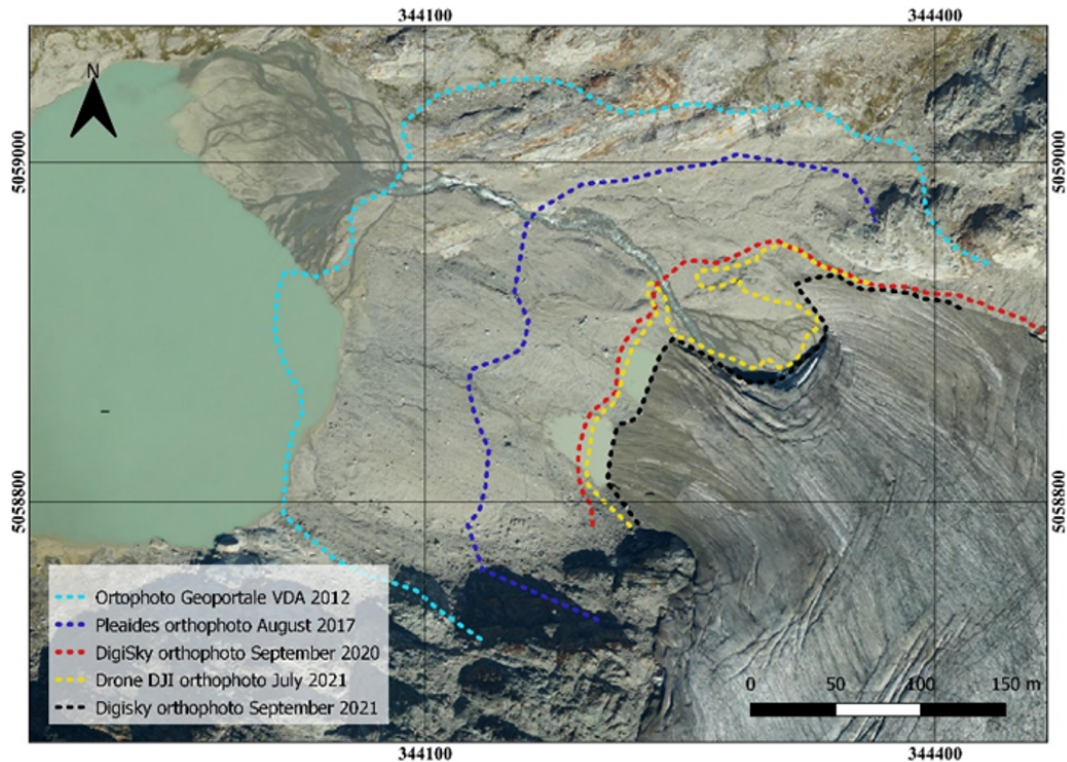


**Figure 8.** Multitemporal analysis of eastern glacial front retreat: front lines plotted on September 2021 ortophoto.

vertical precision (based on CPs) of the DSMs is 11.1 cm for 2021 and 16.7 cm 2020. The DoD Limit of Detection (LoD) at 68% confidence level is 20 cm ( $\sqrt{11.1^2 + 16.7^2}$ ).

**Table 5.** Elevation differences (DSM 2020 - DSM 2021) on stable areas.

Elevation difference (DSM 2020- DSM 2021) on stable areas	
<u>Median</u>	<u>-0.098 m</u>
<u>Mean</u>	<u>-0.082 m ± 0.788 m</u>
<u>Standard deviation (95% confidence level)</u>	<u>0.072 m ± 0.141 m</u>

Figure 9 (a) shows the differences between the 2021 and 2020 DSMs adopting a LoD threshold of 95% = 40 cm (Azmoon et al., 2022). The same elevation profile has been calculated from 2020 and 2021 is DSMs and compared in Figure 9 (b) and (c). Both profiles show a decrease of the glacier surface in the three glacial tongues (the central one is shown in Figure 9 (c)) and throughout the lower part of the glacier, with the most significant decrease in the central and eastern (about 4 meters difference).

390 ~~Additionally, a comparison with the 2008 DSM shows a lowering of glacier surface up to 50 meters in glacial front areas.~~

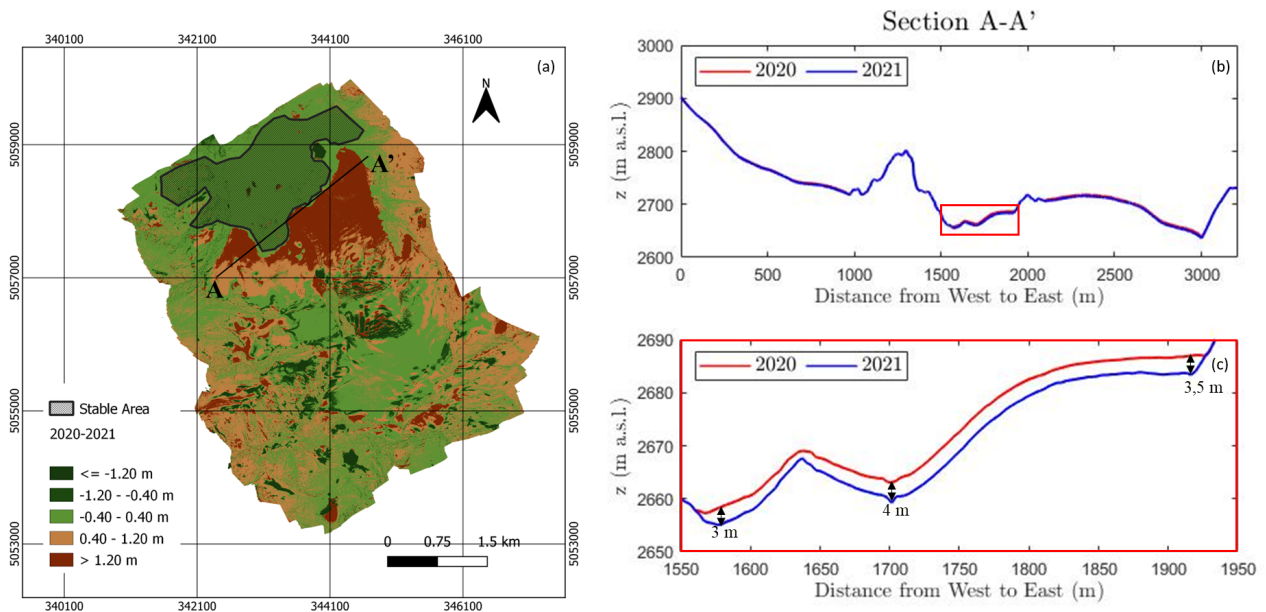


**Figure 9.** (a) Difference between the DSM of 2020 and 2021. The black line refers to the cross-section A-A', whose 2020 (red) and 2021 (blue) elevation profiles are shown in panel (b), with a zoom-in on the central tongue of the glacier in panel (c).

As far as very-high-resolution satellite stereo pairs are concerned, they enable the extraction of 3D information with a lower vertical accuracy (metric level) with respect to aerial and drone data. Nevertheless, the coverage of a much larger area (in the range of hundreds of square kilometres) enables a multiscale and multiplatform approach to identify the most critical areas where to focus the monitoring activities in the field (Macelloni et al., 2022; Giulio Tonolo et al., 2020).

### 395 3.2 Bathymetry and lake bed sediment distribution

The outcome of the GPR survey is a series of georeferenced x-depth sections of the lake. The radar reflections depict two main interfaces: the “water - fine sediments” interface, which represents the lake bottom, and a second deeper interface, which separates the fine sediments from the underlying ground layer. In the example in Figure 10, the first (lake bottom) interface starts at near 0 depth at the left border of the picture, deepening until 250 ns (3.5 m) in the centre of the picture, and then ascending to 0 depth in the right part. The average water depth of the lake was 3.9 meters and the maximum depth was around 11 meters in July 2021. The x-y-z locations of the first interface, representing the lake bottom, detected in all the GPR sections, were interpolated to produce a bathymetry map (Figure 11, which also displays the sediment thickness distribution and the electrical conductivity measurements). The perimeter of the lake, retrieved from the 6-cm-resolution orthophoto, was useful to fix the 0-depth in the interpolation process.

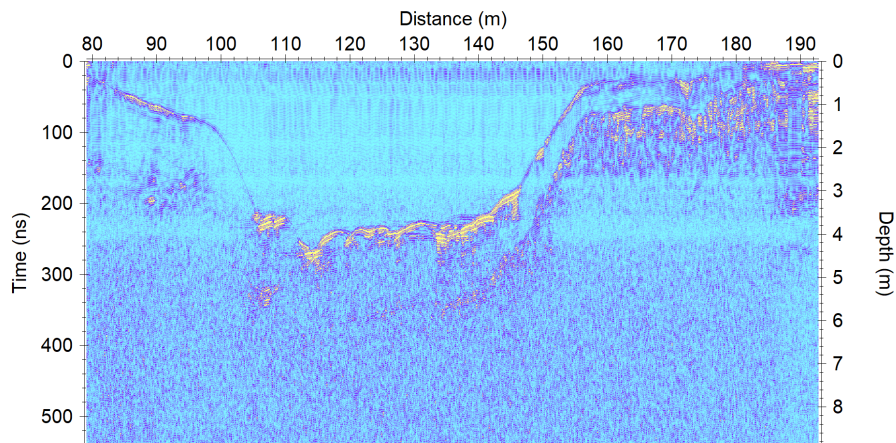


**Figure 10.** Example of a GPR section of the Seracchi Lake. Relevant reflections are the water – fine sediments interface and, deeper, the fine sediments - coarse sediments interface).

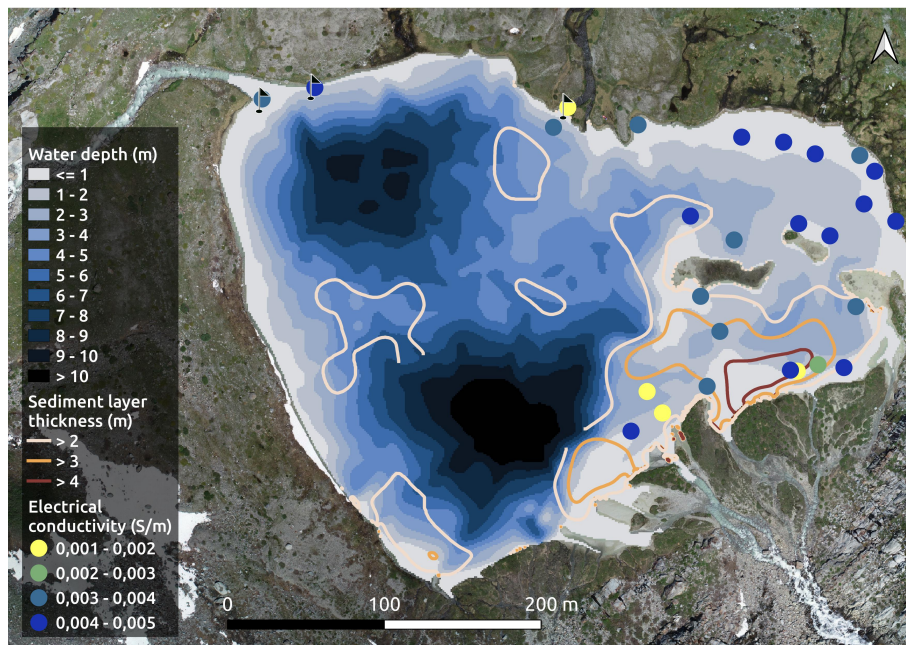


**Figure 11.** Results of the GPR and TDR geophysical survey. In a blue colour scale, the bathymetry of the lake. The brown contour lines indicate the areas where the sediment layer is thicker (in particular near the inflows from the glacier). The yellow-to-blue points indicate the TDR measurements of electrical conductivity. The electrical permittivity is not shown here but it is fairly uniform (average = 36). The three black flags indicate the locations of manual sediment samplings. Colour scale according to Crameri et al. (2020)

405 The deeper interface in Figure 10 is fairly distinguishable and runs parallel to the first interface, deepening until 350 ns. In the left and centre of the image, the sediment thickness is more than double compared to the right part of the image. Under the second interface, many sparse reflections are visible, thus the underlying layer is probably not formed by compact rock, but by coarse debris or sediments, ~~possibly a heterogeneous glacial till~~. The second deeper interface was interpreted as the bottom of the fine sediment layer. To convert the radar two-way travel times to the thickness of this layer, we needed  
410 an estimation of the signal propagation velocity in the fine sediments. The TDR probe measured a fairly uniform average relative electrical permittivity of  $36 \pm 3$ , which was converted to a propagation velocity of about 0.05 m/ns. Similarly to bathymetry, an interpolation process produced a final map of the thickness distribution. Figure 11 shows that a major sediment accumulation has happened in the zones near the glacier inflows (from the Southeast). Aside from this, the fine sediment layer is quite homogeneously distributed all around the lake, with an average of 1.6 meters of thickness. Unfortunately, the zones  
415 where the water was deeper than 6-7 meters could not be penetrated with sufficient energy and the second interface was lost. This is the main limitation of the GPR survey, which restricts its range of applicability to other proglacial lakes, is the depth of investigation. We expect that after 15 meters of depth even the first interface could not be detected anymore, in similar conditions (200 MHz antenna, low-conductivity water).

The TDR probe measured, other than the permittivity, also the electrical conductivity of the sediments. The locations of  
420 measurements, which also correspond to the permittivity measurements, are shown in Figure 10. This property had a uniform value, except in small areas near the inflows. This means that the type of sediment in those zones is different from the rest of the lake. Thanks to sediment sampling (locations in Figure 10) and grain size distribution analysis, together with the electrical conductivity distribution, we reconstructed that the fine sediment layer is fairly uniform around the lake and contains around 50 % of clayish-sized material, while near the inflows there is coarser gravel because the flow velocity does not allow the fine  
425 particles to sediment.

### 3.3 Hydrometric monitoring

~~The ecoLog1000 and CTDs instruments were first installed in July 2021 and June 2022, respectively. The measuring periods of each sensor are shown in a time-measured-quantity diagram in Table 1.~~

~~At The investigation at the L4 gauging station, involved: i a set of 9 velocity-based discharge measurements ( $Q$ ) taken  
430 in the summer of 2021 and 2022 were related to the corresponding water depth measured at the gauge ( $h$ ), in order to plot the which allowed the stage-discharge diagram (Fig. 5(a); details of the procedure followed to determine the stage-discharge relationship are given in Appendix A). Discharge measurements were also used to calibrate the lake outflow curve, i.e., the relationship between the hydraulic head ( $H$ ) in the lake and the flowing discharge (see Fig. 5(c)). For this purpose, a linear fitting between the water depth at the gauge ( $h$ - $Q$ ) to be assessed; ii) a set of 15 elevation difference measurements which  
435 led to the linear fitting (h-H) and the Hydraulic head in the lake-lake outflow curve (H-Q) ( $H$ ) was also calibrated (Fig. 5(b);  $R^2 \sim 0.98$ ), since the water levels in the lake and in the control cross-section in the stream are strictly related but not equal, due to the head-dependant outflow process and water speed (Figure 5).~~

(a) Discharge measurements in L4 emissary and the corresponding water depth (h). (b) Measurements of total head H and the corresponding water depth h. The linear interpolation equation and the coefficient of determination ( $R^2$ ) are reported. (c) Discharge measurements and the corresponding total head H and the stage-discharge curve for L4 emissary.

Thanks to these results it has been possible to reconstruct the high-resolution (10-minute acquisition time) temporal sequence of discharge flowing from the lake and primarily driven by the glacier melt. Figure 12(a) shows this temporal sequence.

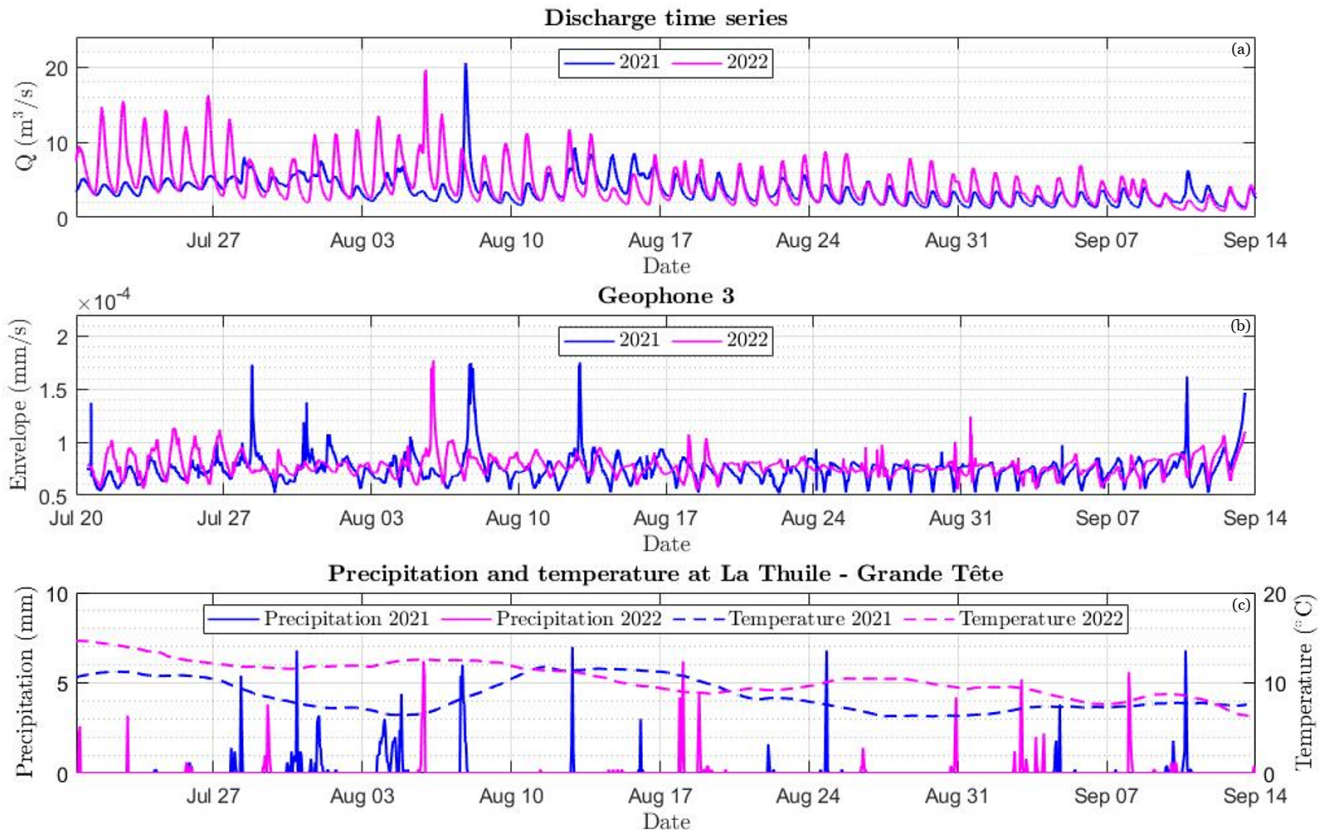


**Figure 12.** (a) Discharge time series in L4 emissary in 2021 and in 2022. (b) Geophone 3 signal envelope in 2021 and in 2022 calculated on a time window of 1-min. (c) Daily precipitation (solid line) and 10-day moving mean of air temperature (dashed-dotted lines) measured at La Thuile-Grande Tête weather station in 2021 and in 2022.

Using meteorological data from the Grande Tête weather station managed by ARPA Valle d'Aosta (data available at [https://presidi2.regione.vda.it/str\\_dataview\\_download](https://presidi2.regione.vda.it/str_dataview_download), last access: 19 January 2023), we observed that water level and water temperature are strongly correlated with air temperature, and this correlation is higher in summer. The average air temperature recorded between May and August summer of 2022 is 3 degrees higher than in has been warmer than that of 2021. Consequently, the average flow measured in July and August in the L4 outfall in 2022 is higher (by 52%) than that measured in 2021 for the same period (by as much as 26%). The difference between the amplitude of the water level fluctuation in 2022 and 2021

is more pronounced in early summer (Fig.Figure 12(a)), due to the different air temperature in May2021 and 2022, which was  
 450 on average 5degrees-°C higher in 2022 than in 2021 (Fig.Figure 12(b)), which led and to an earlier discharge of meltwater in  
 2022 than in the previous year.

The water discharge caused by glacier melt has a strong daily periodicity driven by solar radiation and thermal energy,  
 perturbed occasionally by rainfall events. Unlike the contribution of glacier melt to water discharge, the contribution of rainfall  
 is not periodic within the day, thus altering the otherwise daily periodic flow pattern in glacier-fed watercourses. The auto-  
 455 correlation functions of the water depth time series measured at L4 and L2 highlight the daily periodicity that is strongly  
 related to the glacier melt (Fig.Figure 13 (a) and (b)). However, the amplitude of these functions in 2021 is smaller than in  
 2022 and their daily means cross earlier the zero axis earlier (about 5 days in L4 and 2 days in L2). This fact can be attributed  
 to the different sizes and numbers of precipitation events in the two years (Fig.Figure 12). Rainfall in 2021 was more frequent  
 than in 2022, and the July-August cumulative rainfall was 238,6 mm and 82,6 mm in 2021 and 2022, respectively. Accordingly,  
 460 as the frequency of precipitation increases, the auto-correlation function decreases.

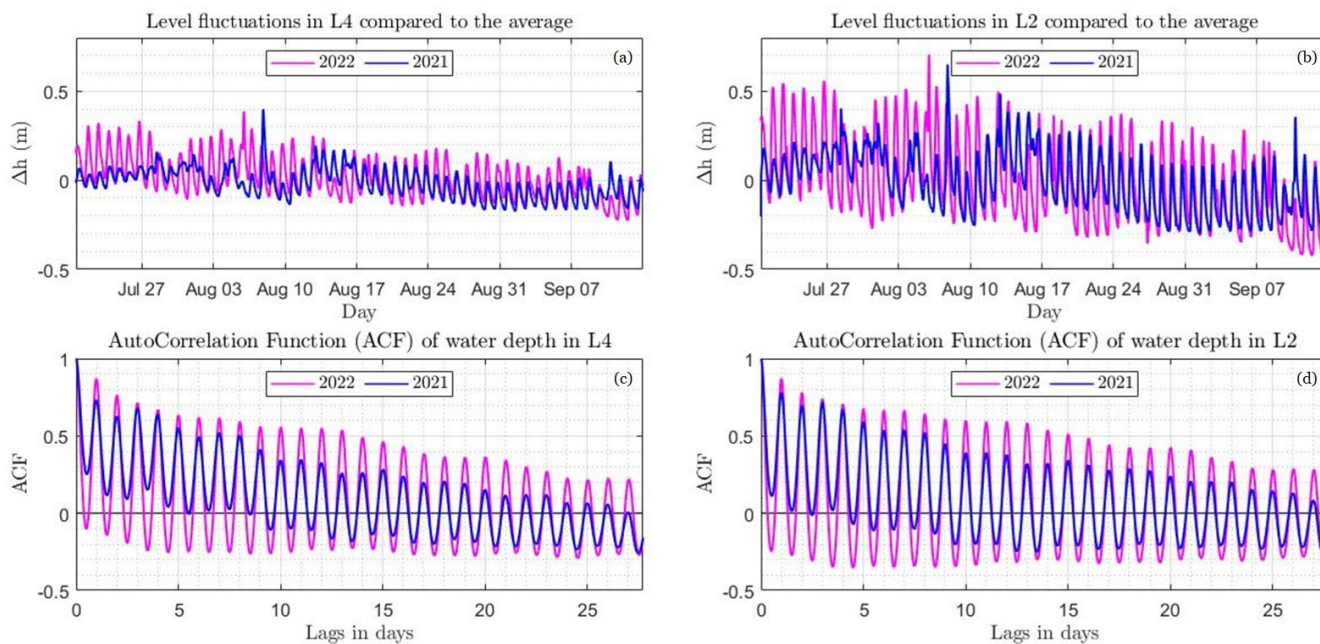


**Figure 13.** Level fluctuations recorded in 2021 (blue) and 2022 (magenta) by measuring stations L4 (a) and L2 (b) and the corresponding autocorrelation function in the panels (c) and (d) respectively.

### 3.4 Bedload monitoring

Preliminary results show how an array of single-component geophones installed close to the flow path can detect both daily and longer-period fluctuations in bedload and water flow. The geophone signal mirrors well the flow of daily cycles with

fluctuations within a period of 24 hours and permits the identification of time intervals characterized by intense transport  
465 (Figure 12b). ~~Raw seismic signals were filtered in the band 5-95 Hz and then the envelope was calculated as the average of the  
absolute value of the filtered signal over a time window of 1 min (Figure 12b).~~

Results highlight the signal fluctuations and suggest that intense runoff with bedload transport occurred during specific  
days (i.e., 13 July, 28 July, 4 August, 7 August, and 12-13 August). The larger flood event was detected on 7 August 2021  
(Figure 14), during which a marked increase of the seismic power was observed (i.e., one order of magnitude) compared to  
470 time periods characterized by low water flow and no bedload transport.

It is assumed that the geophone signal (Figure 12b) permits the identification of time intervals characterised by intense  
transport since, in correspondence with the peaks of the envelope, the power increases for high values of frequency (Figure 14).  
Indeed, the power in the lower bands is attributed to turbulent fluid flow (Schmandt et al., 2013) while that in the higher bands  
to bedload (Schmandt et al., 2013; Bakker et al., 2020).

475 ~~In 2021, we directly observed the absence of bedload transport in three days (2021, we observed, through direct inspection of  
the flow field, the absence of bedload transport in three days (10 July, 20 July and 13 September). During the 2022 season, we  
performed direct measurements of bedload transport at the glacier mouth by means of portable samplers on the occasion of one  
day of intense glacier melt (14 July) and at the end of the monitoring season (16 September). Bedload traps (4 mm mesh size, 20  
× 30 cm opening, (Bunte et al., 2004)) were deployed simultaneously at 2 positions. Measured unit bedload rates feature a large  
480 variability ranging from 0.02 to 16.2 kg/m/min in a few hours, as already observed in glacierized basins (Coviello et al., 2022)  
-. Bedload samples were sieved and weighed to obtain the grain size distribution. The total bedload transport rate  $Q_s$  (kg/min  
above 4 mm) for each sampling period (ranging from 2 to 30 min) was estimated as width-weighted averages based on the  
available positions sampled.~~ The dataset of direct measurements will be expanded in 2023 and used to calibrate the seismic  
data and extract quantitative information on the bedload export from the glacier.



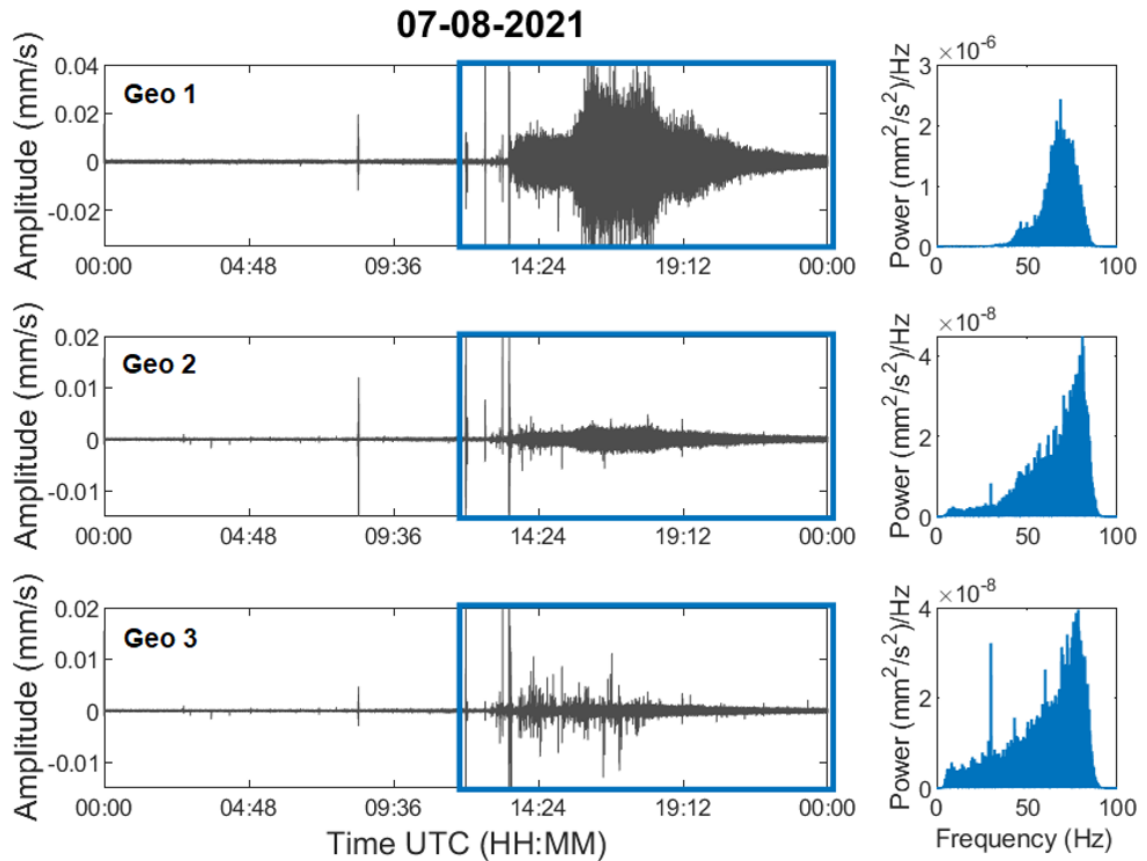


**Figure 14.** Waveforms recorded on 7 August 2021 and power spectra of a specific portion of the signal (blue boxes, from noon to midnight UTC).

485 ~~Five~~

#### 4 Data availability

Eight different datasets were produced. These datasets are listed below and accessible in a WebGIS (available at <https://arcg.is/Tyeju0>, last access: 14 March 2023) through which the link to the open archive can be found according to the location of the monitored/surveyed point:

490 – The orthophotos and DSMs database [related to the 2020 aerial survey](https://zenodo.org/records/8089499) is available on the Zenodo repository at (<https://zenodo.org/records/8089499> ([Corte et al. \(2023d\)](#)));

- [The orthophotos and DSMs database related to the 2021 aerial survey is available on the Zenodo repository at https://zenodo.org/records/10100968](https://zenodo.org/records/10100968) (Corte et al. (2023b));
- 495 – The [orthophotos and DSMs database related to the 2021 UAV survey is available on the Zenodo repository at https://zenodo.org/records/10074530](https://zenodo.org/records/10074530) (Corte et al. (2023b));
- [The Rutor glacier surface area database obtained from the orthophoto of September 2021 is available on the Zenodo repository at https://zenodo.org/records/10101236](https://zenodo.org/records/10101236) (Corte et al. (2023b));
- The footprints of the various glacial fronts obtained from the elaborated cartographic products database is available on the Zenodo repository at <https://doi.org/10.5281/zenodo.7713146> (Corte et al. (2023c))
- 500 – The bathymetry and sediment thickness of L4 database is available on the Zenodo repository at <https://doi.org/10.5281/zenodo.7682072> (Corte et al. (2023a));
- The dataset of the water depth measured by the instrument installed at gauging stations L1, L2, L3 and L4 and the relationship between the water depth and the wetted area at gauging station L4 is available on the Zenodo repository at <https://zenodo.org/record/7697100> (Corte et al. (2023e));
- 505 – The geophones monitoring database is available on the Zenodo repository at <https://doi.org/10.5281/zenodo.7708800> (Corte et al. (2023f)).

Our objective is to increase and update the dataset by continuing to monitor and survey the Rutor ~~Glacier~~ [glacier](#) and its proglacial area over the years through this multidisciplinary approach.

## 5 ~~Discussion and conclusions~~ [Conclusions](#)

510 At present, ~~(to the best of our knowledge, there is)~~ [appears to be](#) a lack of studies in the literature on proglacial areas involving multitemporal geospatial surveys with continuous monitoring [of melt water runoff](#) during the ablation period, which merge the contributions of different disciplines. At the same time, very few cases exist of continuous monitoring of streamflow at high frequency and high altitude.

In this work, a multidisciplinary and multitemporal approach was presented to characterise the Rutor glacier and its proglacial  
515 area. ~~The dataset presented in this paper—completely accessible in a free-access repository as well as through a WebGIS application—includes: a multitemporal geospatial dataset composed by 3D models of the entire glacial and proglacial area at very high spatial resolution and positional accuracy (both in the range of few centimetres and based on different geomatics techniques); a dataset of water depths measured at four different locations within the hydrographic network of the proglacial area with a temporal resolution of 10 minutes and the wetted area associated with different water depths in the cross-section  
520 of L4 outfall; geotechnical analyses performed on the L4 sediments (e.g. particle size distribution and Atterberg limits) and maps of the bathymetry and sediment thickness of L4; geophone data collected along the proglacial stream fed by the right~~

~~tongue of the glacier, which are transformed into signal envelopes computed as the average of the absolute values of the raw data calculated over a 1-minute time window.~~

Multidisciplinary analyses are fundamental in the study of complex environment. It is instructive to summarise some direct  
525 examples of the synergies involved in a multidisciplinary approach for the investigated area. Firstly, the comparison of multi-  
temporal 3D geospatial data determined that the eastern tongue is losing mass faster than the other, leading to the intensification  
of measurements at L1 and nearby the eastern tongue of the glacier. Secondly, the orthoimage based on the photogrammetric  
~~drone-UAV~~ surveys carried out at the same time as the geophysical survey, enabled the accurate extraction of the lake perimeter,  
which - integrated with the data acquired from the GPR - resulted in an accurate bathymetry of the lake and allowed to get  
530 the exact outline of the zero-depth points at the time of the investigation. Thirdly, continuous hydraulic monitoring at the L4  
gauging station and the relationship between the water depth measured by the sensor and the lake's depth provided the volume  
change of L4 over time. In addition, combining the bathymetry map with the DSM of the surrounding area will enable the  
determination of the water volume of L4 when the water level is higher than at the time of the geophysical survey. Lastly, the  
extracted products of the crewed aerial photogrammetric flights allowed the Environmental Agency (ARPA VDA) to develop  
535 the mass balance for the hydrological years under consideration. The comparison of different DSMs sets the basis for continu-  
ous monitoring over time, in which the 2021 model will serve as a reference for future comparisons. The mass balance of the  
Rutor glacier can also be determined through the application of a hydrological model calibrated with the water discharge time  
series obtained from this study. It is important to stress that the accurate georeferencing of all the acquired data with respect to  
the same Datum plays a crucial role in the data integration phase and in enabling the multitemporal analyses.

540 Future modelling of the water flow and sediment transport in L4 may be based on the bathymetry map combined with the  
inflow and outflow measurements. The GPR and TDR surveys, with a few ground-proof sediment sampling, evidenced that  
in about 140 years since the birth of the lake, a fine sediment layer thick 1.6 m on average was deposited on the lake bottom.  
~~The future sediment~~ Sediment transport deserves further investigation, because it may change due to the rapid shrinking of the  
Rutor glacier, whose bedrock erosion is the source of the fine sediment found in the lake. An approach to model these changes  
545 could involve temporal monitoring of water turbidity as a proxy of the concentration of suspended sediment in the various  
inflows and outflows of the interconnected water bodies.

The multidisciplinary approach and the dataset herein presented enable the characterisation, monitoring and understanding  
of a set of complex processes that take place in the studied area, allowing the authors to shed light on interconnected phenomena  
with a broader perspective than a single scientific discipline approach. Indeed, the results of a combined effort often go beyond  
550 the sum of each contribution.

## **Appendix A: Stage-discharge relationship for L4**

The procedure followed to measure the velocity is reported in ISO 748:2007. The methods used to determine the discharge  
from current-meter measurements are classified in ISO 748:2007 as the graphical method and the arithmetic method. The

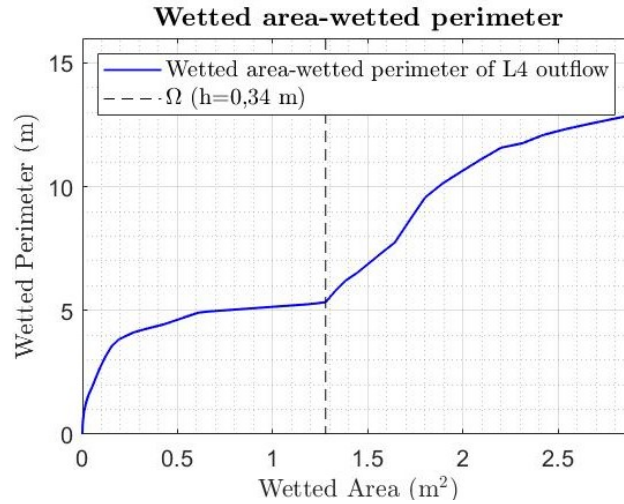


**Figure A1.** The wetted area and the corresponding wetted perimeter for water depths between  $h = 0$  and  $h = 52$  cm.

latter, which is more suitable for computations carried out in the field, includes two methods: the mean-section method and the  
 555 mid-section method. The discharge was determined by applying both arithmetic methods and averaging the two results.

The power law is the one that best represents the stage-discharge measurements (Figure 5):

$$Q = 12.118 \times h^{4.0042}, \quad R^2 = 0.925. \quad (\text{A1})$$

The lowest water discharge measured corresponds to a water depth in the cross-section of 0.49 m. In fact, the power law  
 describes well the  $Q - h$  relationship when  $h$  is greater than half a metre. For shallower water depths, the power law returns a  
 560 flow rate that is too low for the geometry of the cross-section considered. Consequently, for  $h < 0.49$  m, the stage-discharge  
 curve was obtained by taking into account the geometry of the cross-section.

Water discharge can be written as a function of the wetted area of the cross-section:

$$Q = k \times \Omega^m, \quad (\text{A2})$$

where  $Q$  is the discharge,  $k$  is a flow resistance coefficient,  $\Omega$  is the wetted area and  $m$  is a coefficient dependent on the cross-  
 565 section geometry. To obtain the expression of the coefficient  $m$ , the stage-discharge relationship and Chézy's equation were  
 expanded using the Taylor series and set equal each other, thus obtaining:

$$m = \frac{5}{2} - \frac{2}{3} \frac{\Omega_0}{B_0} \left( \frac{dB}{d\Omega} \right)_{\Omega_0}. \quad (\text{A3})$$

This coefficient depends on the wetted area ( $\Omega$ ) and the wetted perimeter ( $B$ ) of the cross-section.

The geometry of the cross-section of L4's emissary was determined through an RTK survey. The measurements of the three  
 570 coordinates of the points within the cross-section bed were with steps of about 20 cm along the cross direction.

When visualizing the cross-section geometry and the curve that describes how the wet perimeter changes with the wet area (Figure A1), it is clear that two different stage-discharge relationships, corresponding to two different water depth intervals, must be considered:

$$Q = k_1 \times \Omega(h)^{m_1}, \quad 0 \text{ m} \leq h \leq 0.34 \text{ m} \quad (\text{A1})$$

$$575 \quad Q = k_2 \times \Omega(h)^{m_2}, \quad 0.34 \text{ m} \leq h \leq 0.49 \text{ m}. \quad (\text{A2})$$

For each interval, the coefficient  $m$  was calculated as the mean of all the values determined at each point within the corresponding interval. Considering the first interval from  $h_1$  to  $h_n$  and the second from  $h_{n+1}$  to  $h_l$ , the coefficients were calculated according to:

$$m_1 = \frac{1}{n} \sum_{i=1}^n \frac{5}{2} - \frac{2}{3} \frac{\Omega_i}{B_i} \left( \frac{dB}{d\Omega} \right)_{\Omega_i}, \quad 0 \text{ m} \leq h \leq 0.34 \text{ m} = 1.487 \quad (\text{A3})$$

$$580 \quad m_2 = \frac{1}{l-n} \sum_{i=n+1}^l \frac{5}{2} - \frac{2}{3} \frac{\Omega_i}{B_i} \left( \frac{dB}{d\Omega} \right)_{\Omega_i} = 1.0609, \quad 0.34 \text{ m} \leq h \leq 0.49 \text{ m}. \quad (\text{A4})$$

The  $k$  coefficients were calculated by imposing the continuity stage-discharge relationship respectively at  $h = 0.34$  cm and  $h = 0.49$  cm, thus obtaining  $k_1 = 0.232$  and  $k_2 = 0.257$ . The definitive stage-discharge relationship is given by three different relationships corresponding to three different water depth intervals:

$$Q = 0.232 \times \Omega^{1.487}, \quad 0 \text{ m} \leq h \leq 0.34 \text{ m} \quad (\text{A5})$$

$$585 \quad Q = 0.257 \times \Omega^{1.069}, \quad 0.34 \text{ m} \leq h \leq 0.49 \text{ m} \quad (\text{A6})$$

$$Q = 12.118 \times h^{4.0042}, \quad h \geq 0.49 \text{ m}. \quad (\text{A7})$$

## A1

### Appendix B: GPR data processing

The GPR profiles were processed in Reflexw software (Sandmeier, 2021) according to the following processing steps:

- 590
- "Move starttime", to delete the data acquired before the radar impulse transmission. To recognize automatically the timing of the transmitted impulse, the ReflexW processing "Correct max phase" was used.
  - "Make equidistant traces", to make every trace distant 0.1 m between each other, to compensate for the variable speed of the boat.
  - "subtract mean - dewow", a filter that subtracted to each trace the average of that trace, on a 5-ns timewindow, to correct

595 for instrumental voltage shifts.

  - "Bandpass butterworth", a bandpass filter which cut the frequencies lower than 50 MHz and higher than 260 MHz.

600

- "subtracting average", a filter that subtracts the average trace from each trace, on a 100-traces window, to eliminate horizontally coherent noise.
- "energy decay", a simple time-axis gain function which equalizes the energy of the traces, which generally decreases over time.

*Author contributions.*

Conceptualization & Supervision (AC, CC, AG, ST); Investigation (All authors); Data Curation (EC, VC, MMM, AV); Visualization (AA, EC, MMM, FGT, AV); EC prepared the manuscript with contributions from all co-authors.

*Competing interests.*

605 The authors declare that no competing interests are present

*Acknowledgements.* We thank Umberto Morra di Cella (ARPA - Valle d'Aosta) for the collaboration and interesting discussions, and Francesco Comiti and Matthias Bonfrisco (Free University of Bozen) for supporting bedload measurements. The research has been funded by the European Union with the Alcotra-Interreg project R.I.T.A and the Italian Ministry for Education and Research (MIUR), through the project "Department of Excellence".

## 610 References

- Alley, R., Cuffey, K., Evenson, E., Strasser, J., Lawson, D., and Larson, G.: How glaciers entrain and transport basal sediment: Physical constraints, *Quaternary Science Reviews*, 16, 1017–1038, [https://doi.org/https://doi.org/10.1016/S0277-3791\(97\)00034-6](https://doi.org/https://doi.org/10.1016/S0277-3791(97)00034-6), 1997.
- ARPA Valle d'Aosta: Bilancio di massa, ARPA Valle d'Aosta, Tech. rep., Agenzia Regionale Protezione Ambiente Valle d'Aosta, <https://www.arpa.vda.it/it/effetti-sul-territorio-dei-cambiamenti-climatici/ghiacciai/bilancio-di-massa>, 2014.
- 615 Azmoon, B., Biniyaz, A., and Liu, Z.: Use of High-Resolution Multi-Temporal DEM Data for Landslide Detection, *Geosciences*, 12, <https://doi.org/10.3390/geosciences12100378>, 2022.
- Bakker, M., Gimbert, F., Geay, T., Misset, C., Zanker, S., and Recking, A.: Field Application and Validation of a Seismic Bedload Transport Model, *J. Geophys. Res. Earth Surf.*, 125, e2019JF005 416, <https://doi.org/https://doi.org/10.1029/2019JF005416>, e2019JF005416 2019JF005416, 2020.
- 620 Baretta, M.: Il ghiacciaio ed i laghi del Rutor, Tipografia Editrice di G. Candeletti, 1880.
- Bogen, J., Xu, M., and Kennie, P.: The impact of pro-glacial lakes on downstream sediment delivery in Norway, *Earth Surf. Process. Landf.*, 40, 942–952, <https://doi.org/10.1002/esp.3669>, 2015.
- Bradford, J. H., Johnson, C. R., Brosten, T., McNamara, J. P., and Gooseff, M. N.: Imaging thermal stratigraphy in freshwater lakes using georadar, *Geophys. Res. Lett.*, 34, L24 405, <https://doi.org/10.1029/2007GL032488>, 2007.
- 625 Bunte, K., Abt, S. R., Potyondy, J. P., and Ryan, S. E.: Measurement of Coarse Gravel and Cobble Transport Using Portable Bedload Traps, *J. Hydraul. Eng.-ASCE*, 130, 879–893, [https://doi.org/10.1061/\(ASCE\)0733-9429\(2004\)130:9\(879\)](https://doi.org/10.1061/(ASCE)0733-9429(2004)130:9(879)), 2004.
- Camporese, M., Penna, D., Borga, M., and Paniconi, C.: A field and modeling study of nonlinear storage-discharge dynamics for an Alpine headwater catchment, *Water Resour. Res.*, 50, 806–822, 2014.
- Carrer, M., Dibona, R., Prendin, A. L., and Brunetti, M.: Recent waning snowpack in the Alps is unprecedented in the last six centuries, *Nat. Clim. Chang.*, pp. 1–6, <https://doi.org/10.1038/s41558-022-01575-3>, 2023.
- 630 Carrivick, J. L. and Tweed, F. S.: Deglaciation controls on sediment yield: Towards capturing spatio-temporal variability, *Earth-Sci. Rev.*, 221, 103 809, <https://doi.org/https://doi.org/10.1016/j.earscirev.2021.103809>, 2021.
- Cavalli, M., Heckmann, T., and Marchi, L.: Sediment Connectivity in Proglacial Areas, pp. 271–287, *Geography of the Physical Environment*, Springer International Publishing, Cham, 2018.
- 635 Chiabrando, F., Giulio Tonolo, F., and Lingua, A.: UAV DIRECT GEOREFERENCING APPROACH IN AN EMERGENCY MAPPING CONTEXT. THE 2016 CENTRAL ITALY EARTHQUAKE CASE STUDY, *Int. Arch. Photogramm. Remote Sens. Spatial Inf. Sci.*, XLII-2/W13, 247–253, <https://doi.org/10.5194/isprs-archives-XLII-2-W13-247-2019,2019>, 2019.
- Corte, E., Ajmar, A., Camporeale, C., Cina, A., Coviello, V., Giulio Tonolo, F., Godio, A., Macelloni, M. M., Oggeri, C., Tamea, S., and Vergnano, A.: Bathymetry, sediment thickness, and geotechnical-geophysical properties of sediments of Lake Seracchi in Rutor proglacial area, Zenodo repository, Dataset, <https://doi.org/10.5281/zenodo.7682072>, last access: 6 March 2023, 2023a.
- 640 Corte, E., Ajmar, A., Camporeale, C., Cina, A., Coviello, V., Giulio Tonolo, F., Godio, A., Macelloni, M. M., Tamea, S., and Vergnano, A.: Orthophoto and DSM Rutor Glacier 2021, Zenodo repository, Dataset, <https://doi.org/10.5281/zenodo.7713299>, last access: 6 March 2023, 2023b.
- Corte, E., Ajmar, A., Camporeale, C., Cina, A., Coviello, V., Giulio Tonolo, F., Godio, A., Macelloni, M. M., Tamea, S., and Vergnano, A.: Rutor glacier fronts footprints, Zenodo repository, Dataset, <https://doi.org/10.5281/zenodo.7713146>, last access: 6 March 2023, 2023c.
- 645

- Corte, E., Ajmar, A., Camporeale, C., Cina, A., Coviello, V., Giulio Tonolo, F., Godio, A., Macelloni, M. M., Tamea, S., and Vergnano, A.: Orthophoto and DSM Rutor Glacier 2020, Zenodo repository, Dataset, <https://doi.org/10.5281/zenodo.8089498>, last access: 24 October 2023, 2023d.
- 650 Corte, E., Ajmar, A., Camporeale, C., Cina, A., Coviello, V., Giulio Tonolo, F., Godio, A., Macelloni, M. M., Tamea, S., and Vergnano, A.: Hydrometric data in the Rutor proglacial area, Zenodo repository, Dataset, <https://doi.org/10.5281/ZENODO.7697100>, last access: 6 March 2023, 2023e.
- Corte, E., Ajmar, A., Camporeale, C., Cina, A., Coviello, V., Giulio Tonolo, F., Godio, A., Macelloni, M. M., Tamea, S., Vergnano, A., Bonfrisco, M., and Comiti, F.: Geophone data in the Rutor proglacial area (Valle d'Aosta, Italy), Zenodo repository, Dataset, <https://doi.org/10.5281/zenodo.7708800>, last access: 6 March 2023, 2023f.
- 655 Coviello, V., Capra, L., Vázquez, R., and Márquez-Ramírez, V. H.: Seismic characterization of hyperconcentrated flows in a volcanic environment, *Earth Surf. Process. Landf.*, 43, 2219–2231, <https://doi.org/10.1002/esp.4387>, 2018.
- Coviello, V., Vignoli, G., Simoni, S., Bertoldi, W., Engel, M., Buter, A., Marchetti, G., Andreoli, A., Savi, S., and Comiti, F.: Bedload Fluxes in a Glacier-Fed River at Multiple Temporal Scales, *Water Resour. Res.*, 58, e2021WR031873, <https://doi.org/10.1029/2021WR031873>, 2022.
- 660 Curry, A. M., Cleasby, V., and Zukowskyj, P.: Paraglacial response of steep, sediment-mantled slopes to post-‘Little Ice Age’ glacier recession in the central Swiss Alps, *J. Quat. Sci.*, 21, 211–225, <https://doi.org/10.1002/jqs.954>, 2006.
- Delaney, I., Bauder, A., Huss, M., and Weidmann, Y.: Proglacial erosion rates and processes in a glacierized catchment in the Swiss Alps, *Earth Surf. Process. Landf.*, 43, 765–778, <https://doi.org/10.1002/esp.4239>, 2018.
- Eichel, J.: *Vegetation Succession and Biogeomorphic Interactions in Glacier Forelands*, pp. 327–349, Springer International Publishing, Cham, [https://doi.org/10.1007/978-3-319-94184-4\\_19](https://doi.org/10.1007/978-3-319-94184-4_19), 2019.
- 665 Giulio Tonolo, F., Cina, A., Manzino, A., and Fronteddu, M.: 3D Glacier Mapping by means of satellite stereo images: The Belvedere glacier case study in the Italian Alps, *ISPRS - International Archives of the Photogrammetry, Remote Sensing and Spatial Information Sciences*, XLIII-B2-2020, 1073–1079, <https://doi.org/10.5194/isprs-archives-XLIII-B2-2020-1073-2020>, 2020.
- Gizzi, M., Mondani, M., Suozzi, E., Glenda, T., and Lo Russo, S.: Aosta Valley Mountain Springs: A Preliminary Analysis for Understanding Variations in Water Resource Availability under Climate Change, *Water*, 14, <https://doi.org/10.3390/w14071004>, 2022.
- 670 GLIMS Consortium, .: *GLIMS Glacier Database, Version 1*, <https://doi.org/10.7265/N5V98602>, 2005.
- Grove, J. M.: *Little Ice Ages. Ancient and Modern: 2nd edition*, Routledge, 2004.
- Guillon, H., Mugnier, J. L., and Buoncristiani, J. F.: Proglacial sediment dynamics from daily to seasonal scales in a glaciated Alpine catchment (Bossons glacier, Mont Blanc massif, France), *Earth Surf. Process. Landf.*, 43, 1478–1495, <https://doi.org/10.1002/esp.4333>,
- 675 2018.
- Hallet, B., Hunter, L., and Bogen, J.: Rates of erosion and sediment evacuation by glaciers: A review of field data and their implications, *Glob. Planet. Change*, 12, 213–235, [https://doi.org/10.1016/0921-8181\(95\)00021-6](https://doi.org/10.1016/0921-8181(95)00021-6), impact of Glaciations on Basin Evolution: Data and Models from the Norwegian Margin and Adjacent Areas, 1996.
- He, H., Aogu, K., Li, M., Xu, J., Sheng, W., Jones, S. B., González-Teruel, J. D., Robinson, D. A., Horton, R., Bristow, K., Dyck, M., Filipović, V., Noborio, K., Wu, Q., Jin, H., Feng, H., Si, B., and Lv, J.: A review of time domain reflectometry (TDR) applications in porous media, in: *Advances in Agronomy*, vol. 168, pp. 83–155, Academic Press Inc., <https://doi.org/10.1016/bs.agron.2021.02.003>, 2021.
- 680



- Heckmann, T. and Schwanghart, W.: Geomorphic coupling and sediment connectivity in an alpine catchment — Exploring sediment cascades using graph theory, *Geomorphology*, 182, 89–103, <https://doi.org/https://doi.org/10.1016/j.geomorph.2012.10.033>, 2013.
- 685 Hicks, D. M., McSaveney, M. J., and Chinn, T. J.: Sedimentation in proglacial Ivory Lake, Southern Alps, New Zealand, *Arct. Alp. Res.*, 22, 26–42, <https://doi.org/10.2307/1551718>, 1990.
- Hilger, L. and Beylich, A. A.: *Sediment Budgets in High-Mountain Areas: Review and Challenges*, chap. 15, pp. 251–269, Springer International Publishing, Cham, [https://doi.org/10.1007/978-3-319-94184-4\\_15](https://doi.org/10.1007/978-3-319-94184-4_15), 2019.
- Hooke, R. L.: Toward a uniform theory of clastic sediment yield in fluvial systems, *GSA Bulletin*, 112, 1778–1786, 690 [https://doi.org/10.1130/0016-7606\(2000\)112<1778:TAUTOC>2.0.CO;2](https://doi.org/10.1130/0016-7606(2000)112<1778:TAUTOC>2.0.CO;2), 2000.
- Ivy-Ochs, S., Kerschner, H., Maisch, M., Christl, M., Kubik, P. W., and Schlüchter, C.: Latest Pleistocene and Holocene glacier variations in the European Alps, *Quaternary Science Reviews*, 28, 2137–2149, <https://doi.org/https://doi.org/10.1016/j.quascirev.2009.03.009>, holocene and Latest Pleistocene Alpine Glacier Fluctuations: A Global Perspective, 2009.
- Laute, K. and Beylich, A. A.: Environmental controls, rates and mass transfers of contemporary hillslope processes in the headwaters of two 695 glacier-connected drainage basins in western Norway, *Geomorphology*, 216, 93–113, <https://doi.org/10.1016/j.geomorph.2014.03.021>, 2014.
- Macelloni, M. M., Corte, E., Ajmar, A., Cina, A., Giulio Tonolo, F., Maschio, P. F., and Pisoni, I. N.: Multi-platform, Multi-scale and Multi-temporal 4D Glacier Monitoring. The Rutor Glacier Case Study, in: *Geomatics for Green and Digital Transition*, edited by Borgogno-Mondino, E. and Zamperlin, P., pp. 392–404, Springer International Publishing, Cham, 2022.
- 700 Mao, L., Comiti, F., Carrillo, R., and Penna, D.: Sediment Transport in Proglacial Rivers, in: *Geomorphology of Proglacial Systems, Geography of the Physical Environment*, pp. 199–217, Springer International Publishing, Cham, 2018.
- Matthews, J. A.: *Geomorphology of Proglacial Systems: Landform and Sediment Dynamics in Recently Deglaciated Alpine Landscapes*, vol. 29 (7), Springer Cham, <https://doi.org/10.1177/0959683619840576>, 2019.
- Matthews, J. A. and Briffa, K. R.: The ‘little ice age’: re-evaluation of an evolving concept, *Geogr. Ann. Ser. A-Phys. Geogr.*, 87, 17–36, 705 <https://doi.org/10.1111/j.0435-3676.2005.00242.x>, 2005.
- Moreau, M., Mercier, D., Laffly, D., and Roussel, E.: Impacts of recent paraglacial dynamics on plant colonization: A case study on midtre Lovénbreen foreland, Spitsbergen (79°N), *Geomorphology*, 95, 1-2 : 48-60., *Geomorphology*, 95, 48–60, <https://doi.org/10.1016/j.geomorph.2006.07.031>, 2008.
- Müller, B. U.: Paraglacial sedimentation and denudation processes in an Alpine valley of Switzerland. An approach to the quantification of 710 sediment budgets, *Geodin. Acta*, 12, 291–301, [https://doi.org/10.1016/S0985-3111\(00\)87046-1](https://doi.org/10.1016/S0985-3111(00)87046-1), 1999.
- Orombelli, G.: Il ghiacciaio del Rutor (Valle d’Aosta) nella piccola era glaciale, *Geogr. Fis. Din. Quat.*, 2005.
- Orwin, J. F. and Smart, C. C.: Short-term spatial and temporal patterns of suspended sediment transfer in proglacial channels, small River Glacier, Canada, *Hydrol. Process.*, 18, 1521–1542, 2004.
- Psarras, G. C.: Fundamentals of dielectric theories, in: *Dielectric Polymer Materials for High-Density Energy Storage*, pp. 11–57, Elsevier, 715 <https://doi.org/10.1016/B978-0-12-813215-9.00002-6>, 2018.
- Raup, B. H., Racoviteanu, A., Khalsa, S. S., Helm, C., Armstrong, R., and Arnaud, Y.: The GLIMS geospatial glacier database: A new tool for studying glacier change. *Global and Planetary Change*. 56., <https://doi.org/10.1016/j.gloplacha.2006.07.018>, 2007.
- Sacco, F.: Il ghiacciaio ed i laghi del Rutor, vol. 36, Provveditorato generale dello stato, 1917.
- Sambuelli, L., Colombo, N., Giardino, M., and Godone, D.: A waterborne GPR survey to estimate fine sediments volume and find optimum 720 core location in a Rockglacier Lake, in: *Near Surface Geoscience 2015 - 21st European Meeting of Environmental and Engineering*

- Geophysics, 1, pp. 811–815, European Association of Geoscientists and Engineers, EAGE, <https://doi.org/10.3997/2214-4609.201413826>, 2015.
- Sandmeier, K.-J.: Reflexw, <https://www.sandmeier-geo.de/index.html>, 2021.
- Schmandt, B., Aster, R. C., Scherler, D., Tsai, V. C., and Karlstrom, K.: Multiple fluvial processes detected by riverside seismic and infrasound  
725 monitoring of a controlled flood in the Grand Canyon, *Geophys. Res. Lett.*, 40, 4858–4863, <https://doi.org/10.1002/grl.50953>, 2013.
- SCT Geoportale, Regione autonoma Valle d’Aosta: <https://mappe.regione.vda.it/pub/geonavitg/geodownload.asp?carta=DSM08>.
- Slaymaker, O.: Criteria to Distinguish Between Periglacial, Proglacial and Paraglacial Environments, *Quaest. Geogr.*, 30, 85–94, <https://doi.org/doi:10.2478/v10117-011-0008-y>, 2011.
- Sommer, C., Malz, P., Seehaus, T., Lippl, S., Zemp, M., and Braun, M. H.: Rapid glacier retreat and downwasting throughout the European  
730 Alps in the early 21st century, *Nat Commun*, 11, <https://doi.org/10.1038/s41467-020-16818-0>, 2020.
- Strigaro, D., Moretti, M., Mattavelli, M., Frigerio, I., Amicis, M. D., and Maggi, V.: A GRASS GIS module to obtain an estimation of glacier behavior under climate change: A pilot study on Italian glacier, *Comput. Geosci.*, 94, 68–76, <https://doi.org/10.1016/j.cageo.2016.06.009>, 2016.
- Teppati Losè, L., Chiabrando, F., and Giulio Tonolo, F.: ARE MEASURED GROUND CONTROL POINTS STILL RE-  
735 QUIRED IN UAV BASED LARGE SCALE MAPPING? ASSESSING THE POSITIONAL ACCURACY OF AN RTK MULTI-ROTOR PLATFORM, *Int. Arch. Photogramm. Remote Sens. Spatial Inf. Sci.*, XLIII-B1-2020, 507–514, <https://doi.org/10.5194/isprs-archives-XLIII-B1-2020-507-2020>, 2020a.
- Teppati Losè, L., Chiabrando, F., and Giulio Tonolo, F.: Boosting the Timeliness of UAV Large Scale Mapping. Direct Georeferencing Approaches: Operational Strategies and Best Practices, *ISPRS International Journal of Geo-Information*, 9,  
740 <https://doi.org/10.3390/ijgi9100578>, 2020b.
- Valbusa, U. and Peretti, L.: *Relazioni delle Campagne Glaciologiche del 1936*, vol. 17, Tipografia Nazionale di G. Bertero e C., 1937.
- Vergnano, A., Oggeri, C., and Godio, A.: Geophysical–geotechnical methodology for assessing the spatial distribution of glacio-lacustrine sediments: The case history of Lake Seracchi, *Earth Surface Processes and Landforms*, 2023.
- Villa, F., De Amicis, M., and Maggi, V.: GIS analysis of Rutor Glacier (Aosta Valley, Italy) volume and terminus variations, *Geogr. Fis. Din. Quat.*, 30, 87–95, 2007.
- Zhang, T., Li, D., East, A. E., Walling, D. E., Lane, S., Overeem, I., Beylich, A. A., Koppes, M., and Lu, X.: Warming-driven erosion and sediment transport in cold regions, <https://doi.org/10.1038/s43017-022-00362-0>, 2022.